SAND2022-12821

SANDIA REPORT
SAND20XX-XXXX
Printed September 2022

Sandia National Laboratories

Full 3D Kinetic Modeling and Quantification of Positive Streamer Evolution in an Azimuthally Swept Pin-to-Plane Wedge Geometry

Ashish K. Jindal, Christopher H. Moore, Andrew S. Fierro, and Matthew M. Hopkins

Prepared by
Sandia National Laboratories
Albuquerque, New Mexico
87185 and Livermore,
California 94550

Issued by Sandia National Laboratories, operated for the United States Department of Energy by National Technology & Engineering Solutions of Sandia, LLC.

Available to DOE and DOE contractors from
U.S. Department of Energy
Office of Scientific and Technical Information
P.O. Box 62
Oak Ridge, TN 37831

Telephone: (865) 576-8401
Facsimile: (865) 576-5728
E-Mail: reports@osti.gov
Online ordering: http://www.osti.gov/scitech

Available to the public from
U.S. Department of Commerce
National Technical Information Service
5301 Shawnee Rd
Alexandria, VA 22312

Telephone: (800) 553-6847
Facsimile: (703) 605-6900
E-Mail: orders@ntis.gov
Online order: https://classic.ntis.gov/help/order-methods/

ABSTRACT

Cathode-directed streamer evolution in near atmospheric air is modeled in 3D pin-to-plane geometries using a 3D kinetic Particle-In-Cell (PIC) code that simulates particle-particle collisions via the Direct Simulation Monte Carlo (DSMC) method. Due to the computational challenges associated with a complete 360° volumetric domain, a practical alternative was achieved using a wedge domain and a range of azimuthal angles was explored (5°, 15°, 30°, and 45°) to study possible effects on the streamer growth and propagation due to the finite wedge angle. A DC voltage of 6 kV is administered to a hemispherical anode of radius 100 μm, with a planar cathode held at ground potential, generating an over-volted state with an electric field of 4 MV/m across a 1500 μm gap. The domain is seeded with an initial ion and electron density of 10^{18} m^{-3} at 1 eV temperature confined to a spherical region of radius 100 μm centered at the tip of the anode. The air chemistry model [1] includes standard Townsend breakdown mechanisms (electron-neutral elastic, excitation, ionization, attachment, and detachment collision chemistry and secondary electron emission) as well as streamer mechanisms (photoionization and ion-neutral collisions) via tracking excited state neutrals which can then either quench via collisions or spontaneously emit a photon based on specific Einstein-A coefficients [2, 3]. In this work, positive streamer dynamics are formally quantified for each wedge angle in terms of electron velocity and density as temporal functions of coordinates r, ϕ, and z. Applying a random plasma seed for each simulation, particles of interest are tracked with near femtosecond temporal resolution out to 1.4 ns and spatially binned. This process is repeated six times and results are averaged. Prior 2D studies have shown that the reduced electric field, E/n, can significantly impact streamer evolution [4]. We extend the analysis to 3D wedge geometries, to limit computational costs, and examine the wedge angle's effect on streamer branching, propagation, and velocity. Results indicate that the smallest wedge angle that produced an acceptably converged solution is 30°. The potential effects that a mesh, when under-resolved with respect to the Debye length, can impart on streamer dynamics and numerical heating were not investigated, and we explicitly state here that the smallest cell size was approximately 10 times the minimum λ_D in the streamer channel at late times. This constraint on cell size was the result of computational limitations on total mesh count.

This page left blank

CONTENTS

LIST OF FIGURES

LIST OF TABLES

ACRONYMS AND DEFINITIONS

Abbreviation	Definition
3D	Three dimensional
PIC	Particle-In-Cell
DSMC	Direct Simulation Monte Carlo
DC	Direct Current
r	Radial coordinate in cylindrical coordinate system
ϕ	Azimuthal coordinate in cylindrical coordinate system
z	Axial coordinate in cylindrical coordinate system
2D	Two dimensional
λ_D	Debye length
N_2	Diatomic nitrogen
UV	Ultraviolet
O_2	Diatomic oxygen
MCC	Monte Carlo Collision
FEM	Finite Element Mesh
ρ	Charge density
ε	Permittivity
V	Electrostatic potential
$\boldsymbol{E}^n$	Electric Field and n^{th} time step
n	Refers to the n^{th} time step
Δt	Time step
i	Refers to the i^{th} charged particle
$\boldsymbol{v}_i$	Velocity of the i^{th} charged particle
m_i	Mass of the i^{th} charged particle
q_i	Total charge of the i^{th} charged particle
$\boldsymbol{F}_i$	Force exerted on the i^{th} charged particle
VHS	Variable Hard Sphere
N	Atomic nitrogen
O	Atomic oxygen
A	Particles of species A
N_A	Number of computational particles of species A
V_{cell}	Volume of a mesh cell
w	Particle weight

Abbreviation	Definition
B	Particles of species B
N_c	Number of candidate computational particles for collision
Ω_{AB}	Interaction factor for collision between particle species A and B
N_B	Number of computational particles of species B
v_r	Relative speed between particles of species A and B
σ_{tot}	Total interaction cross section between particles
σ_{VHS}	Cross section for Variable Hard Sphere Collision
w_j	Weight of j^{th} particle
w_k	Weight of k^{th} particle
j	Refers to j^{th} interaction particle
k	Refers to k^{th} interaction particle
R_1	Random number between 0 and 1
τ_r	Lifetime of an excited state
R_0	Uniformly distributed random number between 0 and 1
t	Time coordinate
Δx	Smallest mesh element size
dz	Incremental distance in the axial direction
dr	Incremental distance in the radial direction
Φ	Total azimuthal wedge angle
E_ϕ	Component of the electric field along the azimuthal direction
$d\phi$	Incremental distance in the azimuthal direction

1. INTRODUCTION

In contrast to Townsend breakdown, an alternative operating regime where space charge effects can significantly distort the local field of an electron avalanche, can exist. Under these conditions, the phenomena of streamers emerge as precursors to complete ionized channel formation, whereby the gap between two conductive surfaces is electrically shorted. Due to their role in a wide variety of applications including surface flashover [5], breakdown in liquids [6, 7], automotive spark-plugs [8], combustion [9], switches [10], sprites and lightning [11, 12, 13, 14], and medicine [15], streamers are gaining momentum as an important area of scientific study.

Streamers are generally classified into two categories – negative, or anode-directed, and positive, or cathode-directed. Anode-directed streamers propagate in the direction of electron drift and do not require a continual source of new electrons ahead of the streamer front to grow since electrons from the ionized region of the streamer can drift in the direction of the field. Cathode-directed streamers on the other hand propagate in a direction opposite the electron drift velocity and therefore require a continual source of fresh electrons ahead of the streamer front to grow. The origin of this source is often fueled by photoionized electrons ahead of the streamer front that generate electron avalanches or "branches" that propagate back to the streamer head, and ultimately merge into the main "trunk" of the streamer. These electron avalanches are the result of electrons that enter the high field region near the streamer head and rapidly multiply due to electron-impact ionization. In nitrogen-oxygen mixtures such as air, the photoionized electrons that are responsible for this process are born as a result of N_2 molecules that are initially excited and then emit UV-photons in the 98 to 102.5 nm range, capable of ionizing O_2 molecules. In this paper, we present the evolution of positive streamers due to the fact that they form more readily in air [16].

We present here three-dimensional simulations in near atmospheric pressure air as part of a two-fold effort, comprised of pushing the boundaries and fidelity of current streamer simulations achievable via the use of massively parallel processing, and to determine if any 3D streamer effects would be vital to advancing our understanding of streamer discharge dynamics. It was not known *a priori* what wedge size (azimuthal angle), if any, would strike a sound balance between computational efficiency and 3D dependent discharge behavior.

Our approach is distinctly *dissimilar* to various *classes* of 3D studies that have used:

a) a fluid model of the drift-diffusion reaction type in a uniform background field generated by a parallel-plate like geometry [17, 18, 19, 20, 21],
b) a fluid model in a rod-plane configuration characterized by a non-uniform background field [22],
c) a PIC-MCC (Monte Carlo Collision) method in a uniform background field that does not take into account the time delay between generation of an excited state and the creation of a photoionized electron-ion pair [23],
d) both PIC [24] and PIC-MCC [25, 26] methods where electrons are modeled as particles while ions are immobile and included as fluid-based densities alongside a homogenous stationary background of neutral gas molecules,
e) a PIC-MCC approach comprised of coupling 2D-axisymmetric coordinates with a quasi 3D approach during the initial stages of streamer development [27],
f) a hybrid approach for negative streamers that excludes photoionization, such that electrons in high field and low density regions are treated as particles but coupled with a fluid model for the remainder of the domain [28, 29, 30], and

g) an iterative method that solves the discretized elliptic Poisson equation in either matrix or equation forms where photoionization is modeled with a homogenous electron density [31].

Although one of the most similar models used a 3D implicit PIC code where fully kinetic Monte Carlo treatment was applied to all particle interactions in electronegative gases, the method was still MCC and while specifics of the implementation were not provided in the paper, typically MCC methods conserve only mass and charge in the their collisions [32], and not momentum or energy. In order to conserve charge, momentum, and energy (as DSMC does), one must solve the fluid equations for the evolution of the background gas in a coupled hybrid scheme, which introduces its own challenges.

In [33] a fully kinetic PIC-DSMC approach was used with a 10° wedge to model streamer dynamics in a nitrogen/helium gas mixture. However, they acknowledged the question of whether the small wedge angle was sufficient for capturing the 3D effects of streamer dynamics or if the streamer plasma formation would exhibit additional asymmetric 3D features if a full 360° domain had been possible to simulate. Furthermore, since 2D-axisymmetric simulations innately impose ϕ-symmetry, any 3D effects in this coordinate are entirely neglected as it is not possible to capture variations along phi. Imposing such a restriction has the potential to adversely affect streamer evolution in other directions as well. In this paper, we will show that ϕ-directed streamer branching is in fact strongly influenced by the wedge angle.

Figure 1 serves to exemplify our computational capabilities in which electric field and electron density distributions are shown along various dimensions for 5° and 30° wedges. We present this "result" in this introductory section to better prepare the reader for the metrics and model setup we describe in more detail below. Specifically, the magnitude of the electric field and electron density are overlaid on top of one another along a vertical slice in the r-z plane, spatially located at the midsection of each wedge. For visual clarity, the vertical slice has been *artificially* oriented to lie in the plane that is the rear vertical face of each wedge (i.e., ϕ = 5°, 30°), explaining the more pronounced planar tilt shown for 30°. The electron density distribution in the r-ϕ plane is also shown at four different heights above a planar cathode located at z = 0, namely 700, 900, 1100, and 1300 μm. A pin-shaped anode is located 1500 μm above the cathode surface. Although addressed in greater detail in the discussion to follow, it suffices here to note that the electric field and hence streamer evolution follow a more off-axis path for the 5° case, while greater on-axis propagation is observed at 30°. The latter case is representative of 15° and 45° as well. The bending of the electric field contours as they approach the cathode is expected in order to satisfy boundary conditions requiring orthogonal termination at a perfect conductor boundary condition.

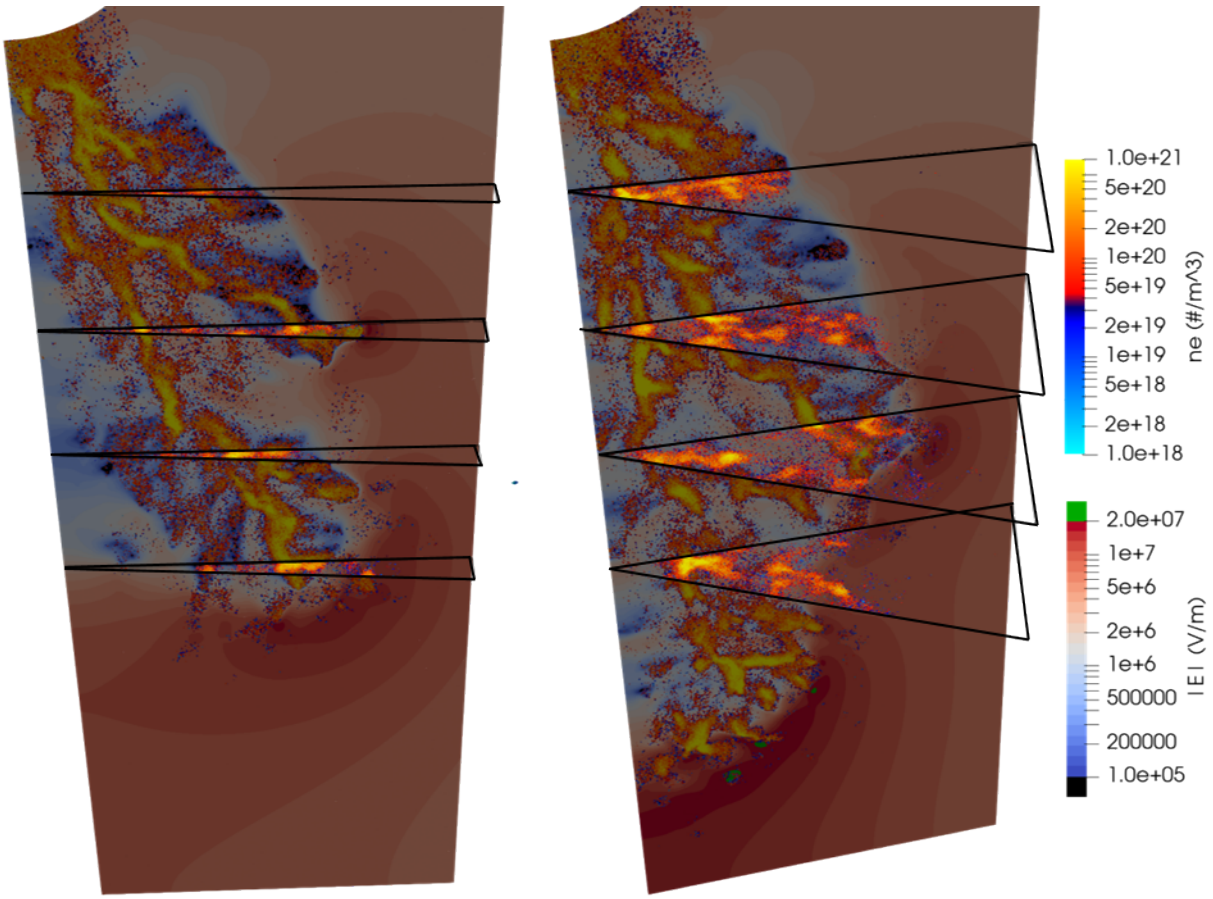

Figure 1. Electric field magnitude and electron density (both log scales) are shown along the vertical slice taken through the midsection (here the angle is swept from -ϕ/2 to +ϕ/2, where the mid-plane is at ϕ = 0) of 5° and 30° wedges at 1.4 ns. The electron density is projected on perpendicular horizontal triangular sections bisecting the wedge in the *r*-ϕ plane at *z* = 700, 900, 1100, and 1300 μm above the cathode (bottom most edge of vertical slice). The vertical slice has dimensions of 600 μm (*r*) x 1500 um (*z*), the latter representing the pin (anode) to plane (cathode) distance. The vertical slice for each wedge angle has been oriented such that it lies in a plane tangential to the back face of the wedge, strictly for visual clarity. The 30° case shown here is representative of 15° and 45°.

2. COMPUTATIONAL MODEL

Streamer physics is modeled using a Sandia National Laboratories developed code, Aleph [34], a particle-in-cell (PIC) [35] direct simulation Monte Carlo (DSMC) [36] electrostatic Poisson solver employing an unstructured finite element mesh (FEM). Aleph [34] is designed to support parallel processors on the order of tens of thousands with element and particle counts on the order of 1 billion and 1 trillion [33], respectively, with the versatility to model 1D, 2D and full 3D domains.

2.1. Particle Pushing

The Lorentz forces imposed on particles and the subsequent velocities they acquire are determined by solving for the irrotational electric field from Poisson's equation

$$\nabla \cdot \boldsymbol{E}^n = \nabla \cdot [\, -\nabla \mathrm{V}] = \frac{\rho^n}{\epsilon} \tag{1}$$

where ρ, ε, V, and $\boldsymbol{E}^n$ represent the charge density, permittivity, electrostatic potential, and electric field at the n^{th} time step, respectively. Using a Verlet Leapfrog approach with a simulation time step of Δt, the i^{th} charged particle velocity $\boldsymbol{v}_i$ at the $n+\frac{1}{2}$ time step is calculated via the Lorentz Force on the particle (in the absence of a magnetic field)

$$m_i \frac{\boldsymbol{v}_i^{n+\frac{1}{2}} - \boldsymbol{v}_i^n}{\Delta t/2} = \boldsymbol{F}_i^n = q_i \boldsymbol{E}^n \tag{2}$$

where m_i, q_i, and $\boldsymbol{F}_i$ are the mass, charge, and force on the i^{th} particle, respectively. The new particle velocity is subsequently used to update the position of the i^{th} particle, x_i, at the n+1 time step

$$\frac{x_i^{n+1} - x_i^n}{\Delta t} = \boldsymbol{v}_i^{n+1/2} \tag{3}$$

The updated particle positions are then mapped as discrete particle charges via a mesh-conforming charge density, and the finite element method is invoked to subsequently update the electric fields everywhere on the mesh by evaluating **Error! Reference source not found.**. Applying the formulation of **Error! Reference source not found.**, the velocity at the n+1 time step is then determined using the updated electric fields, and the process is iterated

$$m_i \frac{\boldsymbol{v}_i^{n+1} - \boldsymbol{v}_i^{n+\frac{1}{2}}}{\Delta t/2} = \boldsymbol{F}_i^{n+1} = q_i \boldsymbol{E}^{n+1} \tag{4}$$

2.2. Air Chemistry

The air chemistry model is comprised of standard Townsend breakdown mechanisms including electron-neutral elastic, excitation, ionization, attachment, and detachment collision chemistry and secondary electron emission, as well as streamer mechanisms including photoionization and tracking excited state neutrals that can either quench as a result of collisions with background neutrals (with an assumed probability of quenching, P_{quench} = ½), or spontaneously radiate a photon, auto-dissociate,

or auto-ionize based on transition-specific Einstein-A coefficients [2, 3]. Additionally, ion-neutral (and neutral-neutral) collisions are included.
Photons are modeled as discrete particles that move and stochastically collide through a simulation time step, like other particles in the domain. Diatomic nitrogen and oxygen are assumed to be the dominant species for heavy-heavy particle interactions including elastic collisions via the Variable Hard Sphere (VHS) model [36], quenching, and charge exchange [37] collisions. We utilize a simple approximate model for quenching where 50% of the elastic collisions between an excited and ground state neutral result in quenching the excited state to ground and the energy is converted into relative kinetic energy of the collision pair. Dry air is modeled but N-N, N-O, and O-O interactions are excluded as those collision rates are several orders of magnitude smaller than the included reactions. Anisotropic scattering [38] is used to model all electron-neutral collisions, including both atomic and diatomic nitrogen and oxygen. These collisions include elastic, excitation (electronic, vibrational, and rotational), attachment (3-body and dissociative), and ionization comprised of single (from ground state), multi-step (from metastable states), double, and dissociative types. Dissociative recombination via electron-ion collisions with N_2^+ and O_2^+ ions is also included, along with electron detachment due to negative O_2^- anion-metastable collisions governed by a detachment cross section [4].

2.3. Particle Interactions

In the PIC-DSMC technique, the number of real (physical) particles of each species are spatially tracked over an elemental grid and are represented by a reduced number of "super-particles" within each grid cell in order to constrain the problem space within realizable computational limitations, such as computer memory. Real particles are converted to super, or computational particles, via a weighting scheme, such that the number of computational particles of species A, for example, occupying a grid cell is described by

$$N_A = \frac{n_A V_{cell}}{w} \tag{5}$$

where n_A, V_{cell}, and w are the density of real particles of species A, the volume of a mesh cell, and the particle weight, respectively.

A more detailed description of kinetic interactions can be found in [33] and is therefore only summarized here. Applying the modified No Time Counter (NTC) method [39], the collision of particle species A with another species B is governed by a process that randomly selects the number of candidate particles, N_c, to pair via the following,

$$N_c = \Omega_{AB} \frac{N_A N_B (w \cdot v_r \cdot \sigma_{tot}(v_r))_{max}}{V_{cell}} \tag{6}$$

where Ω_{AB}, N_A, N_B, V_{cell}, w, v_r, σ_{tot} represent an interaction factor, number of computational particles of species A, number of computational particles of species B, the computational particle weight, the volume of the mesh cell, the relative speed between particles A and B, and total interaction cross section, respectively. Here, Ω_{AB} takes on values of either $1/2$ or 1 depending upon whether the same ($A = B$) or different ($A \neq B$) particle species are interacting, respectively. The sum of all interaction cross sections (e.g. inelastic, elastic, excitation, single ionization, etc.) is represented by σ_{tot}. On the contrary, traditional DSMC does not use the sum of all the cross sections (i.e., σ_{tot}), but instead uses σ_{VHS}, since the VHS (Variable Hard Sphere) cross section is calibrated to match viscosity, etc. at low

temperatures. The expression $(w \cdot v_r \cdot \sigma_{tot})_{\max}$ represents the maximum value of $(\min(w_j, w_k) \cdot v_r \cdot \sigma_{tot})$, sampled at each timestep by randomly selecting particle pairs (j,k) from A and B particle species residing within a given cell. N particle pairs (j,k) are then chosen but are only allowed to collide if

$$R_1 < \frac{(min(w_j, w_k) \cdot v_r \cdot \sigma_{tot})}{(w \cdot v_r \cdot \sigma_{tot})_{max}} \quad 7$$

Here R_1 is a uniform random number between 0 and 1. In the event that an interaction is comprised of particles with different computational weights, the more heavily weighted particle is divided into two computational particles, comprised of one that is equal in weight to the particle being collided against, and the other taking on the remainder of the weight in order to conserve mass. The resulting collision is only between the computational particles of equal weight.

2.4. Photonic Mechanisms

As a detailed treatise describing the kinetic modeling of photon mechanics is already provided elsewhere [3, 33], the topic is only briefly summarized here. In the present model, computational photons are generated after a computational excited state atom or molecule spontaneously decays, radiating a computational photon. The resulting wavelength of the created photon is dependent upon the transition energy, transition rate, and emitter velocity. An excited electronic state emits if the following condition is realized,

$$R_0 < 1 - e^{-\frac{\triangle t}{\tau_r}} \quad 8$$

where Δt is the simulation time step, τ_r is the lifetime of an excited state, and R_0 is a uniformly distributed random number between 0 and 1. The direction of an emitted photon is sampled from an isotropic distribution and the corresponding wavelength is associated with a Voigt distribution characterized by gas temperature, T_g, and Einstein coefficient for spontaneous emission, A, where $A = 1/\tau_r$.

Unlike some 3D PIC-MCC models where the time delay between generation of an excited state via collision and emission of a photon is assumed to be zero [23, 25], our discrete approach accurately models these timescales. In [25], the authors point out the following assumption and corresponding uncertainty with their model: the delay between the generation of an excited state and the emission of a UV-photon is assumed to be zero because they are "unaware" of good data on the delay. We believe this assumption is a questionable approximation for studying initiation of streamers on timescales (nanoseconds) that are shorter than typical allowed optical transition lifetimes (~10 ns). If we assume every excited state decays instantly, this will lead to the generation of an unrealistically large population of photons, higher rates of photoionization, and subsequently higher electron densities, which can ultimately mask the actual stochastic initiation and propagation of the streamer.

Transition rates are governed by transition-specific Einstein-A coefficients [2, 3], creating a competitive process between the rates of excited state quenching via collisions and spontaneous emission to multiple different lower states. Some the transition energies are energetic enough to cause photoionization. We track transitions for N_2, O_2, N, and O between various excited states and lower excited states. Spontaneous emission of photons that are below the ionization energy of O_2 (12.071 eV) cannot photoionize and are therefore ignored for computational efficiency, but the state-to-state

transition is captured such that correct branching ratios are obtained for states that decay via multiple pathways.

2.5. Mesh and Boundary Conditions

The initial seed electron responsible for generating an avalanche of electrons that is the precursor to the space charge and field distortion needed for streamer initiation could potentially be realized by the presence of stray cosmic rays. However, to reduce the computational expense associated with the very early processes leading up to streamer initiation, including the development of an initial electron avalanche growing towards the anode, the simulation domain is seeded with an initial plasma density at time $t = 0$. This seed plasma is comprised of 10^{18} m^{-3} electrons with $T_e = 1$ eV, and an equal number of ions at $T_i = 300$ K. Their positions are uniformly randomly distributed in a 100 μm radius sphere placed at the tip of a hemispherical shaped anode (100 μm radius of curvature) separated 1500 μm from a planar cathode. The background gas is 600 Torr (atmospheric pressure in Albuquerque, New Mexico) of 300 K "air" consisting of an 80%/20% molar mixture of N_2 and O_2. The discharge is operated in a strongly over-volted mode with a constant 6 kV DC potential on the anode, generating a bulk electric field of 4 MV/m across the gap. This is sufficient to stimulate rapid initiation and evolution of a positive (cathode-directed) streamer. Table 1 provides a summary of some estimated plasma and numerical parameters that constrain the problem domain. The stated Debye length of 0.235 μm is based on an average electron temperature and density in the streamer front of approximately 0.5 eV and 5 x 10^{20} m^3, respectively.

Full kinetic modeling of all particle species, including electrons, ions, neutrals (atoms, molecules, and excited states), and photons, is enforced, thereby improving the accuracy in characterizing any non-Maxwellian behavior such as that present in the head of the streamer front. Full 3D kinetic modeling is nonetheless subject to its own set of obstacles, such as the challenge to adequately resolve spatial scales like the Debye length, λ_D. We have shown previously [40] that if the Debye length is "modestly" unresolved (e.g., $1 < \Delta x/\lambda_D < \sim 10$) that the streamer velocity and electron densities are slightly affected; however, the overall streamer characteristics and dynamics are not significantly impacted by meshes moderately larger than the Debye length, especially over the short time scales of streamer *initiation* [4]. However, in simulations where the streamer is allowed to grow until the formation of a full spark closes the gap, the electron density continues to grow (i.e., λ_D becomes increasingly smaller, $\Delta x/\lambda_D > \sim 10$) and ultimately reaches a threshold where the effects of an under-resolved mesh on streamer dynamics and numerical heating can no longer be ignored. This is not the case for the simulations discussed herein. Furthermore, in terms of the 3D wedges used in the current study, we expect that the numerical error due to an under-resolved element size, with respect to the Debye length, should be independent of wedge angle. The element size and meshing algorithm were the same for all wedge angles. An additional challenge involves achieving temporal resolution that accurately characterizes high pressure plasma dynamics, such as those associated with large plasma and collision frequencies which required timesteps on the order of femtoseconds. These small timesteps coupled with element counts on the order of 100 million (for 45° wedge) still required computational run times spanning 48 hours on up to 10k cores, to produce approximately 1.5 ns of physical simulation time.

A uniform-sized tetrahedral mesh with $\Delta x = \sim 2.97$ μm elements was applied to a region bounded by the pin anode, the cathode, and from the wedge axis of symmetry to an outer radius of 600 μm (see Figure 2). Outside of this region a non-uniform mesh that gradually increases in size radially outward

from element to element by a Δx multiplicative factor of ~1.04 across a 2400 μm (*r*) x 3000 μm (*h*) region. We denote these as the inner and outer regions, respectively (see Figure 2). A planar cross section of a wedge with dimensions and boundary conditions are shown in Figure 2**Error! Reference source not found.** along with an unstructured tetrahedral mesh used for a 45° 3D wedge simulation in Figure 3. All element sizes in the figure have been increased by a factor of 4 to enhance the clarity of elements. Such an unstructured mesh further reduces computational expenses by improving the effectiveness of the mesh in the simulation domain, providing finer elements in the region of streamer propagation and coarser elements where no or minimal plasma formation is expected to occur. The total number of elements resulting from this unstructured approach for 5°, 15°, 30°, and 45° wedges are approximately 12, 36, 72, and 105 million elements, respectively.

Table 1 shows that the Debye length (0.235 μm) in our simulations is approximately 10x that of the minimum element size (2.97 μm). However, it is important to note that because the streamer density rapidly grows with time over an extremely small time scale (~1 nsec in our simulations), the mesh size to Debye length criteria is only violated for a very short period of time near the end of the simulation and confined to the relatively small region predominantly near the streamer head and throughout the streamer channel. The density grows as photoionized electrons drift back towards the streamer head, producing numerous avalanches in their path. The authors are currently working on simulations investigating the effects that violating the Debye length has on numerical heating, with a subsequent paper to eventually be published.

The boundary conditions applied to the domain are also shown in Figure 2, comprised of Dirichlet at the anode and cathode of 6 kV and 0 V, respectively, and Neumann ($\frac{\partial E}{\partial n} = 0$) everywhere else. To prevent neutral species from leaving the domain, they diffusely scatter at 300K off the anode and cathode and specularly reflect off all other boundaries. Electrons, ions, and photons are only subject to specular boundaries along the two sidewalls of the wedge and the axis of symmetry. They leave the simulation domain upon contact with the anode, cathode, and all remaining surfaces of the wedge.

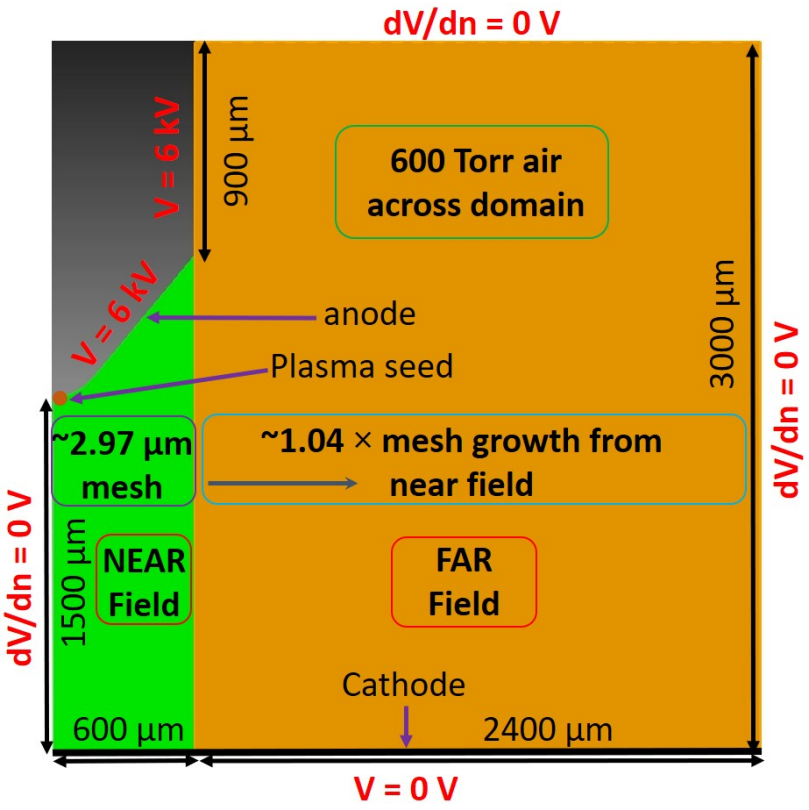

Figure 2. Planar cross-sectional view of a 3D wedge with dimensions and boundary conditions.

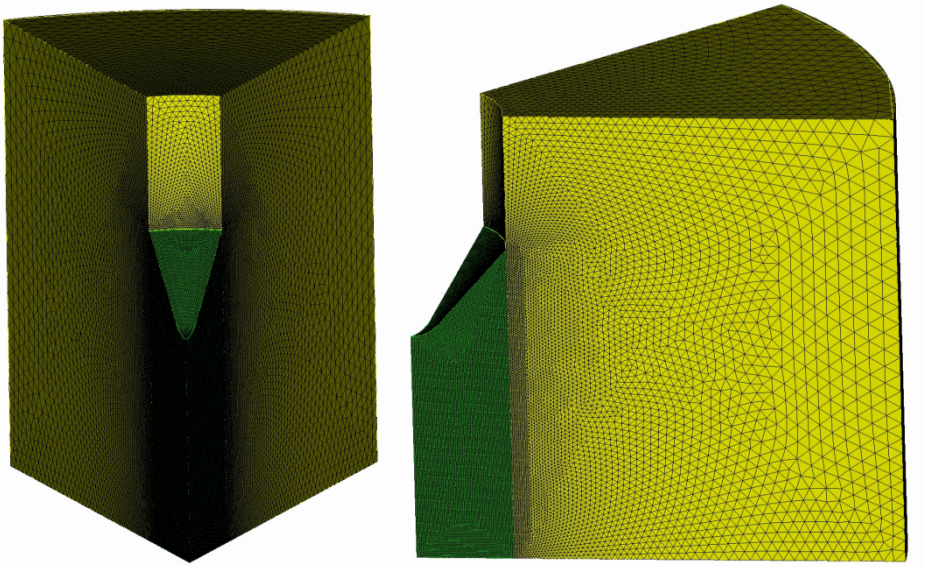

Figure 3. 3D 45° wedge with unstructured tetrahedral mesh used for the plasma simulation. A factor of 4 increase in element size has been applied here strictly for the purpose of improving visual clarity.

Table 1. Estimated plasma and numerical parameters that constrain the simulation numerical parameters.

Parameter	Symbol	Value
Debye length[a]	λ_D	0.235 μm
Electron MFP[b]	λ_e	0.470 μm
Photon Ionization MFP[c]	λ_p	42 μm
Inverse plasma frequency[d]	ω_{pe}^{-1}	5 x 10^{-12} s
Inverse electron collision frequency[e]	υ_c^{-1}	1 x 10^{-12} s
Simulation time step	Δt	5 x 10^{-14} s
Smallest element size	Δx	2.97 μm

[a] Evaluated at an electron temperature and density of 0.5 eV and 5 x 10^{20} m^{-3}, respectively.

[b] Evaluated at 600 Torr gas pressure, maximum $\sigma_{cs} \approx$ 10^{-19} m^2 for elastic electron scattering against N_2

[c] Evaluated at 600 Torr gas pressure, p_{O_2}= 21.2%, maximum σ_{cs}= 5.25 x 10^{-21} m^2 for photoionization of O_2

[d] Evaluated at an electron density of 5 x 10^{20} m^{-3}

[e] Evaluated at 600 Torr gas pressure, $\sqrt{\frac{8k_bT_e}{\pi m_e}}$ = 4.74 x 10^5 m s^{-1}, T_e = 5800 K

3. RESULTS AND DISCUSSION

The effects of both random seed generation in which the spatial positions of electrons and ions are randomly oriented in the spherical seed plasma and the stochastic determination of electron-neutral collisions and spontaneous emission times are averaged over six simulations in the quantitative analysis to follow. The number of real electrons for each wedge angle are spatially tracked and counted throughout the domain by binning them along the directions of the three coordinates r, ϕ, z as functions of time in the near field region, as shown previously in Figure 2. A 15° wedge will contain one-half and one-third the initial electron count from the plasma seed compared to 30° and 45° wedges, respectively. The ratio of the total number of real electrons in the domain to the initial value from the plasma seed (at time $t = 0$) are presented for selected instances in time. This ratio is plotted at the center location of each bin with open triangles, squares, circles, and stars representing 5°, 15°, 30°, and 45° wedges, respectively (Figure 5 (e), Figure 6, and Figure 7). Apart from the total electron count and ϕ-based plots (Figures 12-15), the colors green, blue, red, and magenta represent 0.2, 0.6, 1.0, and 1.4 nsec instances in time, respectively, for all wedge angles in both z (Figure 6) and r directions (Figure 7).

Figure 4 represents a 3D volume rendered depiction of the electron density at 1.4 nsec against the backdrop of a 45° wedge, where the full geometry of the wedge is shown in order to visualize the location and relative size of the streamer with respect to the wedge. When referenced to Figure 4, the streamer clearly originates from the plasma seed located at the anodic pin and grows in all three coordinate directions but is confined to the near field region of the wedge. At this time it has not yet bridged the 1.5 mm gap from pin to cathode.

Before presenting spatially dependent plots of the number of real electrons, it is informative to observe that the ratio of the *total* number of real electrons to the initial seed value as functions of time, averaged over six randomly seeded simulations, are essentially independent of wedge angle for wedges of approximately 20° and greater, as shown in Figure 5 (e); wedges smaller than this angle exhibit progressively greater departure from the 45° case. The absolute minimum and maximum values taken from all six simulations for the 15° case are presented in the form of uncertainty bars at these time steps, clearly showing that it aligns reasonably well with the larger wedge angles. For visual clarity, similar uncertainty bars are *not* shown for 30° and 45° wedges. To better capture the magnitude of these uncertainty bars for *all* wedge angles and time steps, the results for all six randomly seeded simulations at each wedge angle are also shown in Figure 5 (a-d), along with the absolute minimum and maximum extracted for each wedge angle and time step (over these six simulations) presented in tabular form via Table 2.

Although statistically sound arguments cannot be made for small sample sizes, Table 2 helps illustrate why a 5° wedge, and possibly even 15°, is potentially a sub-optimal choice in comparison to 30° and 45°. Table 2 clearly shows that the absolute *maximum* values at 5° are less than the absolute *minimum* at 45° for all points in time, such that no overlap exists between data sets. In contrast, data overlap exists over all time between 30° and 45°. The same is the case for 15°, with the exception at 0.6 ns, characterized by a difference of only 2.5%.

In Figure 5 (e) the differences between the average value for the 15° wedge and those of the 30° and 45° wedges at times greater than approximately 0.8 nsec could potentially be an artifact of simulation

noise as there is overlap between the maximum value for 15° and the minimum value for 30°. The average values for 5° exhibit an even greater departure from 30° and 45°, an explanation for which can only be qualitatively addressed based on a statistically small population size (six). Due to constraints on the availability of shared machine time at Sandia, only six simulations were conducted for each wedge angle, placing limitations on the accuracy of statistical calculations and thereby the potential interpretation of the temporal behavior observed for 5°. Inspection of Figure 5 (c and d) show that the minimum values over all six simulations for the 30° and 45° cases at 1.4 nsec are 1.41 x 10^4 and 1.39 x 10^4, respectively, both lying above the 5° maximum value of 1.35 x 10^4, shown as an uncertainty bar.

The effects of the various stochastic mechanisms involved in streamer dynamics can potentially become more pronounced, along with an increase in associated degrees of freedom, as the electron population grows through streamer branching. Microscopically, the propagating front of a streamer "trunk" is comprised of numerous tips, each characterized by electric fields of varying magnitude that exceed the background field intensity. Photoionized electrons ahead of these tips are stochastically generated and can develop into local electron avalanches which have the potential to eventually merge with these tips, expanding the streamer trunk in the form of branches. The stochastic growth of each branch can be affected by the location of nearby boundaries in a computational model, and therefore the relative size of the geometric volume in which the streamer is allowed to grow.

Hence, it is possible that the shape of the electron distribution from which the results of Figure 5 are based upon can be influenced by the wedge angle and the exponential growth in electron count with time. Without a statistically large population to draw from, it cannot be ruled out that the distribution associated with a relatively narrow 5° wedge may be dramatically different than those associated with 15°, 30°, and 45° wedges. The larger deviation in density observed with time for the 5° wedge can only suggest that the distribution may be dramatically different. To make the argument, backed by a reasonable level of confidence, would require a much larger set of independent simulations. We intend to investigate the behavior associated with a statistically large population and present our findings in a future paper.

The ratio of the number of real electrons to the initial seed count at $t = 0$ averaged over six randomly seeded simulations as functions of wedge angle, time, and spatial direction along the long axis of the gap and radially in the near field region of the domain are shown in Figure 6

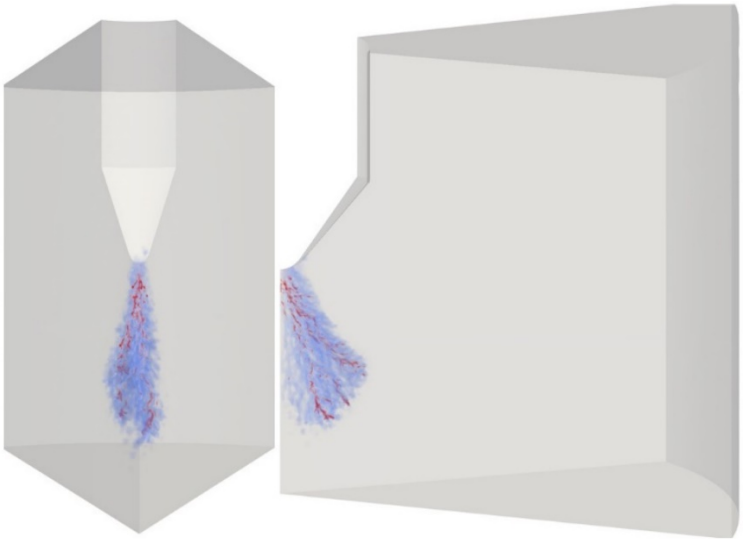

Figure 4. 3D volume render of electron density at 1.4 nsec against backdrop of 45° wedge shown in full dimensions.

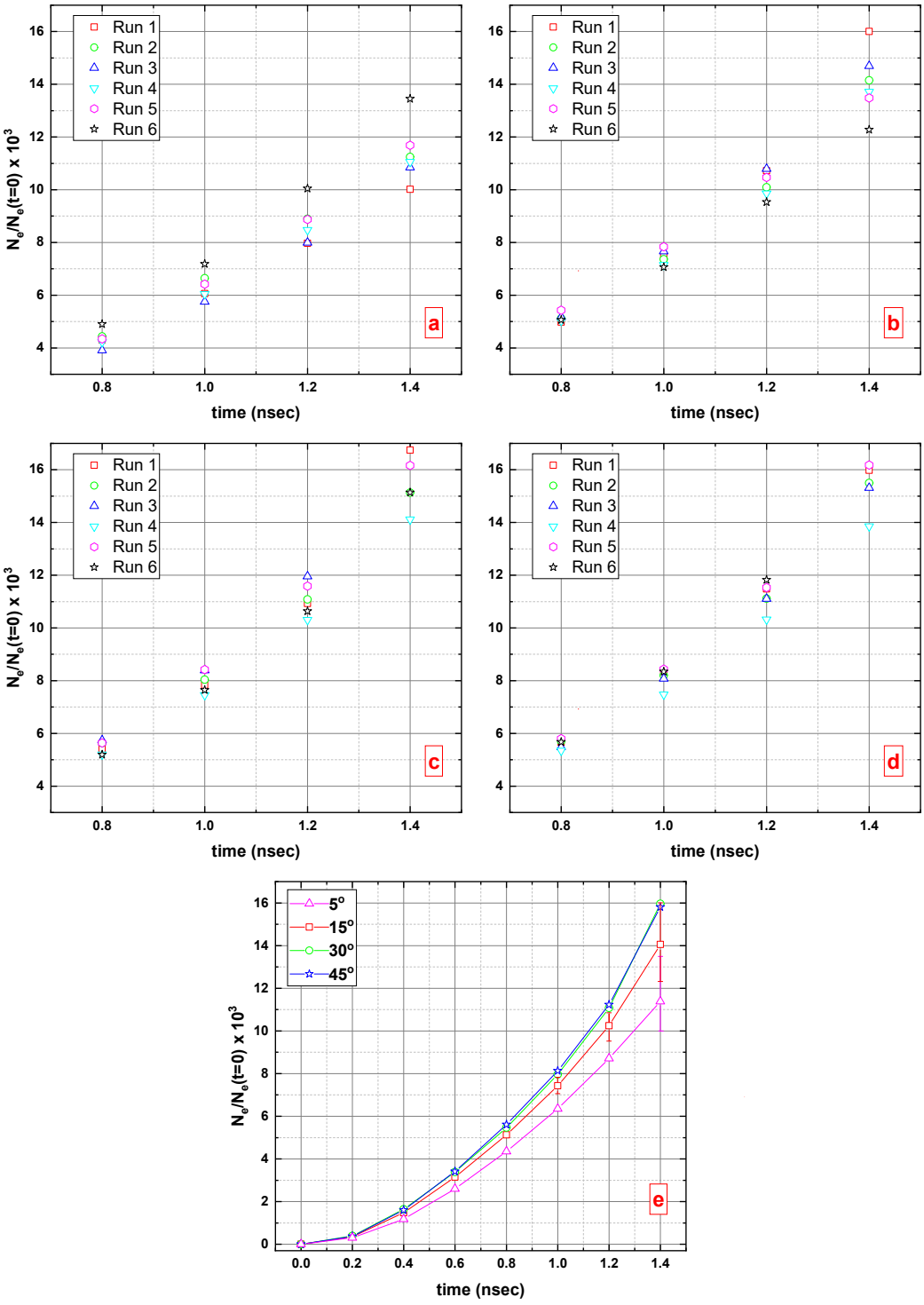

Figure 5. Ratio of total number of real electrons to the initial seed value at time *t* = 0 as functions of time for all six randomly seeded simulations for 5° (a), 15° (b), 30° (c), and 45° (d) wedges and the average values for all wedges (e). The time axis in (a-d) has been truncated to enhance visual clarity of the increased spread in data at late time. Uncertainty bars in (e) represent the absolute minimum and maximum over all six simulations.

Table 2. Uncertainty values represented by the absolute minimum and maximum values of the ratio of total real electrons to the initial count at time $t = 0$ over six randomly seeded simulations, as functions of time and wedge angle. All values shown are to be multiplied by 10^3.

Wedge (°)	0.2ns Min/Max	0.4ns Min/Max	0.6ns Min/Max	0.8ns Min/Max	1.0ns Min/Max	1.2ns Min/Max	1.4ns Min/Max
5	.213/.345	.951/1.42	2.36/2.88	3.90/4.90	5.75/7.18	7.96/10.0	10.0/13.5
15	.307/.382	1.43/1.58	3.08/3.28	4.98/5.43	7.06/7.83	9.53/10.8	12.3/16.0
30	.352/.421	1.42/1.77	3.07/3.58	5.19/5.74	7.45/8.42	10.3/12.0	14.1/18.5
45	.362/.404	1.56/1.70	3.36/3.56	5.35/5.80	7.48/8.44	10.3/11.8	13.9/18.0

And Figure 7, respectively. Electrons are binned in 150 μm and 100 μm increments, representing dz and dr, respectively. In Figure 6, $z = 0$ μm and 1500 μm represent the anode and cathode locations, respectively. In Figure 7, $r = 0$ μm and 600 μm represent the axis of symmetry and the transition region from near to far field, respectively, when referenced to Figure 2. Markers that may be missing at spatial locations near the cathode in Figure 5 (e) simply indicate the absence of electrons.

Similar to Figure 5 (e), the absolute minimum and maximum values over six simulations for the 30° case, for certain distances from the anode, are shown at various times in the form of uncertainty bars in Figure 6 and Figure 7. Uncertainty bars are not shown for other wedge angles simply to reduce excessive clutter and the potential for visual confusion between data sets. The complete set of uncertainty values for *all* wedge angles in the form of absolute minimums and maximums are therefore shown at the same points in time as in Figure 6 and Figure 7 (namely, 0.2, 0.6, 1.0, and 1.4 nsec) for both z and r coordinate directions, in **Error! Reference source not found.**A and **Error! Reference source not found.**A (Appendix), respectively. Based on **Error! Reference source not found.**A (and the error bars for the 30° case in Figure 6), it is apparent that the *delta* between minimum and maximum values, in general, increases with distance from the anode, indicating either an increase in simulation noise with decreasing electron count, or the cumulative effect of many random events for or against ionization, or some combination of the two. With the exception of 5° in Figure 6, the close alignment in the ratios (relative to the bounding uncertainty bars) at each time and spatial location between 15°, 30°, and 45°, spanning a factor of three in total volume, suggests that streamer growth in the axial direction is essentially independent of wedge angle. The values for 5° on the other hand are consistently smaller at times exceeding 0.2 nsec.

What is perhaps more remarkable is that similar behavior is not observed in Figure 7, where the results across all wedge angles align reasonably well. A possible explanation is provided by examining Figure 8, where two representative simulations of the temporal evolution of the electron density and electric field magnitude are plotted in the r-z plane of the near-field region (ie., $0 \leq r \leq 600$ μm of Figure 2), bisecting the wedge at $\phi_0/2$ for the two extreme cases of $\phi_0 = 5°$ (a and b) and $\phi_0 = 45°$ (c and d). The off-axis growth in field and electron density suggest that this is the more preferred path at 5° in comparison to 45°. This effect is most likely an artifact of the extremely limited number of cells that can span a small arc length at 5°, especially along the axis. For a maximum radius of 600 μm in the near field region of the domain, the maximum arc length at 5° is only approximately 52 μm. On the other hand, 52 um of arc length is achieved at approximately 200, 100, and 33 μm radially away from the axis for 15°, 30°, and 45° cases, respectively, corresponding to only 1/3, 1/6, and approximately 1/20 of the total near field radial dimension, respectively. In other words, for the larger wedge angles,

this small arclength can be overcome within a relatively small fraction of the total radial dimension, increasing the volumetric availability and potential for greater z-directed streamer expansion.
Figure 9 presents an axial view looking down from the perspective of the anode, towards the cathode, of the electron density along z planes at axial locations corresponding to **Error! Reference source not found.** (namely 700, 900, 1100, and 1300 μm above the cathode surface) again for the two extreme cases of 5° and 45°, where the right-most edge of each triangle is radially located at 600 μm (at the transition between near and far field boundaries in Figure 2). This view makes more visible the stark contrast in arc length at any radial location from the axis between the two cases, clearly demonstrating streamer expansion while maintaining close proximity to the axis for the largest wedge angle. Due to the extremely narrow azimuthal gap at 5°, it is difficult to definitively state that the streamer is completely filling the azimuthal dimension between the radial edges of the triangle, while it is readily apparent at 45°.

It may at first appear that the streamer is preferentially growing near the bottom radial edge ($\phi = 0$) when inspecting the density profile of the 45° case at 900 μm (circled in red). This could potentially raise the concern that the periodic boundaries along these two radial edges of the triangle (i.e., vertical faces of the 3D wedge) are influencing growth in a non-physical manner. To address this concern, the electron density at 900 μm for the 45° wedge is shown for all six randomly seeded simulations in the right-most column. It appears that, from these six images, streamer growth does not artificially prefer any particular boundary.
Although the evolution of streamers is a stochastic process, as can be seen by the electron density distribution along the r-z plane bisecting each wedge angle at $\phi = \phi_0/2$ (ie., 2.5°, 7.5°, 15°, and 22.5°) at 1.4 nsec for each of six randomly seeded simulations in Figure 10, the results support the prior discussion that streamers are biased to grow more off-axis for 5° wedge domains as it is distinctively observed for each simulation. Similarly, the greatest on-axis growth is most consistently observed for 30° and 45°, while 15° appears to exhibit slightly more fluctuation between runs (e.g., Runs 1 and 5). A statistically large size of simulations would of course be needed to draw a more definitive conclusion.

Axially-directed streamer velocities, presented in Table 3, for 5°, 15°, 30°, and 45° wedges were also evaluated, based on the data in Figure 6, by taking the difference in axial distance traversed by the streamer over 0.4 nsec temporal windows, for two different ratios (10 and 100) of the real number of electrons to the initial seed count at t=0. The velocities certainly lie well within the $10^7 - 10^8$ cm s^{-1} range reported in the literature for positive streamers propagating in air-like chemistries and pressures [16, 23, 41, 42, 43, 44]. The slightly larger values for the 30° case are probably not real and can be attributed to simulation noise. This is evidenced by the spatial overlap between the 30° case and the other wedge sizes, illustrated by the minimum and maximum error bars shown in Figure 6 at each instant in time.

Figures 11-14 depict the temporal distributions in the number of real electrons, scaled by the initial seed count at time $t = 0$, as a function of the azimuthal angle for 5° (Figure 11), 15° (Figure 12), 30° (Figure 13), and 45° (Figure 14) wedges, respectively. Since binning is now in ϕ, the total number of electrons is evaluated in the volume created by sweeping the r-z (out to r=600 μm) plane over an incremental angle, $d\phi$. With the exception of 5° (Figure 11), where the ϕ bin size ($d\phi$) is 1°, $d\phi$ for 15° (Figure 12), 30° (Figure 13), and 45° (Figure 14) wedges are each 3°, such that the *number* of bins now vary as $\Phi/d\phi$, where Φ is the total wedge angle. The top six graphs in each figure represent the

temporal azimuthal distribution resulting from a different random plasma seed (located at the anode as described in Section 2.3), and the bottom most isolated graph represents the average of all six simulations. We attribute the decrease in the maximum $\frac{N_e}{N_{et=0}}$ ratio with increasing Φ to the enhanced ability of the streamer to spread and branch in ϕ. Hence, the scales for all wedge angles have been adjusted accordingly to better capture variations in ϕ. As Φ increases and the volume available for streamer expansion in ϕ follows, an almost discernable double-headed streamer appears to emerge in a few of the 30° plots (Figure 13), and is clearly visible in many of the graphs associated with the 45° (Figure 14). On the other hand, no streamer branching is discernable from any of the plots associated with 5° (Figure 11) and 15° (Figure 12). The results suggest that a 30° wedge may provide the minimum wedge angle necessary to achieve ϕ-directed branching and associated azimuthal features.

Figure 15 is a representative plot of the electron density (a) and ϕ-component of the electric field (E_ϕ) (b) in the near-field region (ie., $0 \leq r \leq 600\ \mu m$ of Figure 2) of the r-ϕ plane located z = 900 μm above the surface of the cathode (z = 0 μm) for 5° and 30° wedges, at 1.4 nsec. It is readily apparent from the figure that $E_\phi \sim 0$ in the elements adjacent to the $\phi = 0$ and $\phi = \phi_0$ (i.e., 5° and 30°) boundaries due to the enforced Neumann condition (ie., $E_\phi = dV/dn = 0$) on those elements' nodes which lie on the boundaries. More importantly, particularly for the 5° case, it is evident that E_ϕ is also approximately 0 within the space near the axis confined by the ϕ = 0° and 5° boundaries and radial distance between r = 0, and ~200 μm, with very weak fields observed as far as ~400 μm in radial extent. Radial distances at 200 and 400 μm from the vertical axis of the wedge (at r = 0) have been delineated by white dashed arcs in Figure 15 (a). It should be noted that the rightmost edge of the wedge, representing the r = 600 μm radial position, appears to be a straight vertical line (instead of an arc) simply due to the magnification used. The expected curvature at this location can be clearly seen in Figure 3 and Figure 4. The lack of E_ϕ and ϕ-directed streamer branching observed for the 5° case (Figure 11) are related and we see that the 30° wedge angle allows non-zero E_ϕ much closer to the axis and thus also ϕ-directed streamer branching. For the 5° case in Figure 15 (a), the pronounced electron density observed at a radial distance of ~275 μm (from r = 0) spans the azimuthal width of the wedge, equating to an azimuthal feature size of ~25 μm; on the contrary, electron density features of the about the same azimuthal size are observed at a much smaller radial distance of ~50 μm (from r = 0) for the 30° case. It is possible that if the near-field region of the domain were expanded beyond 600 μm in radial extent for the 5° wedge, there would be a point at which the streamer would begin to evolve more axially with increasing arc length, due to the expanding volume available for growth. This preferred off-axis growth is corroborated by the decreasing z-directed velocity with time for the 5° case shown in Table 3, along with the data in Figure 6, where the growth rate in $\hat{z}$ at 5° is consistently less than all other wedge sizes at times exceeding 200 psec.

However, it is possible that streamer growth dynamics could change if true periodic boundaries were applied to the vertical faces of each wedge at $\phi = 0$ and $\phi = \phi_0$ (i.e., 5°, 15°, 30°, and 45°), instead of Neumann boundaries, such that a non-zero E_ϕ component of the field could be supported at these boundaries. E_ϕ would effectively be forced to be equal at each corresponding point on the either side of a ϕ-boundary (i.e., $\phi = 0$ and $\phi = \phi_0$) but each element face's E_ϕ on a particular ϕ-boundary could be different from the others and would be self-consistently computed at each field solve timestep. This could potentially improve the likelihood for expansion and branching in ϕ due to the increased

probability of locally photo-ionized electrons generating ϕ-directed avalanches that ultimately merge with the growing streamer trunk. Without simulation results using true periodic boundaries, it is difficult to assess if this would make a difference at all at 5°, due to the extremely restricted arc length as discussed previously.

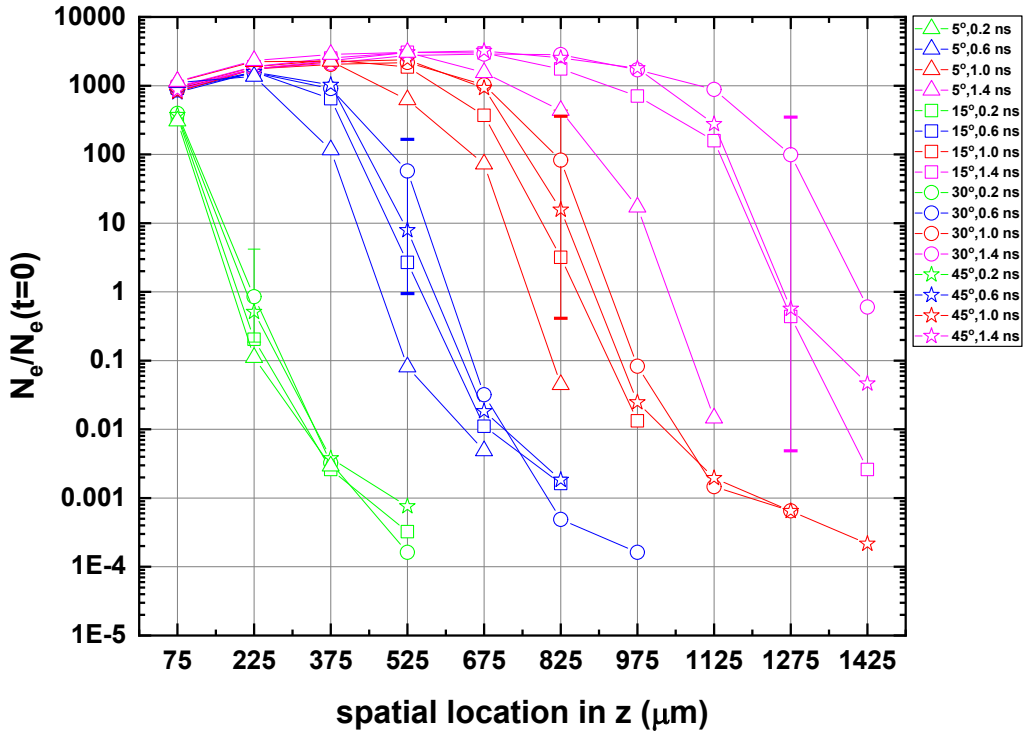

Figure 6. Ratio of the number of real electrons to the initial seed count at $t = 0$ averaged over six randomly seeded simulations as functions of wedge angle, time, and spatial direction in z, binned in 150 μm increments.

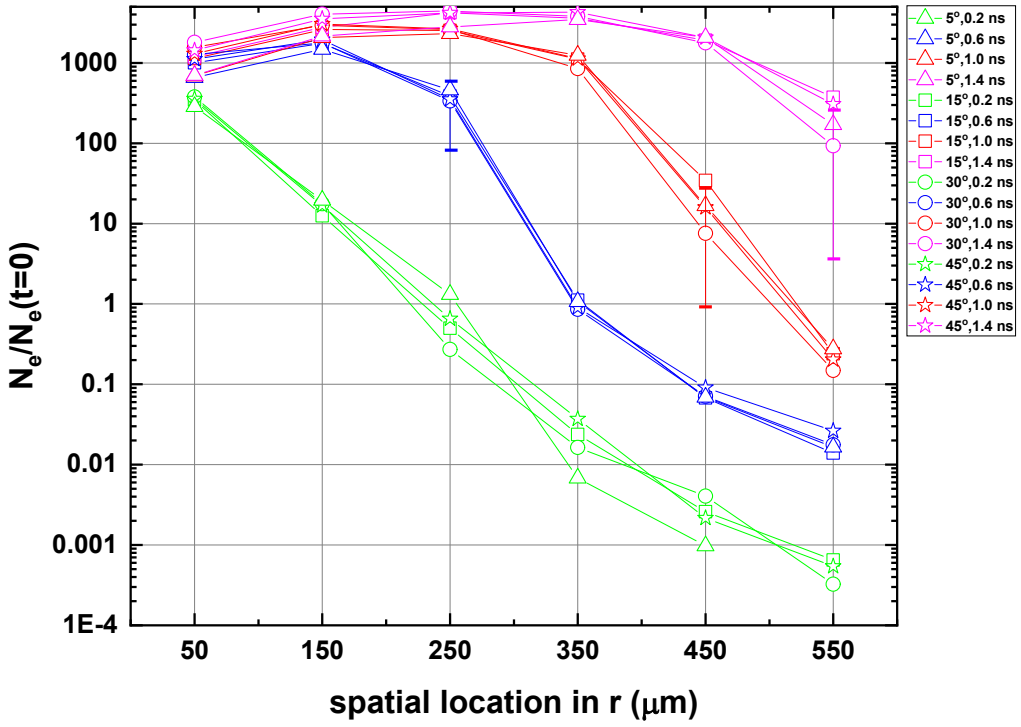

Figure 7. Ratio of the number of real electrons to the initial seed count at *t* = 0 averaged over six randomly seeded simulations as functions of wedge angle, time, and spatial direction in *r*, binned in 100 μm increments.

Table 3. *Z*-directed streamer velocities for 5°, 15°, 30°, and 45° wedges over various Δt = 0.4 nsec windows, evaluated using the ratio of the number of real electrons to initial seed count of both 10 and 100. All velocities shown are to be multiplied by 10^7 cm/s.

Wedge Angle	$\frac{N_e}{N_{et=0}} = 10$			$\frac{N_e}{N_{et=0}} = 100$		
(°)	0.2-0.6 ns	0.6-1.0 ns	1.0-1.4 ns	0.2-0.6 ns	0.6-1.0 ns	1.0-1.4 ns
5	7.15	7.23	6.78	7.05	6.88	6.00
15	8.55	7.50	10.2	8.15	7.25	10.5
30	9.88	7.78	11.8	9.63	8.00	11.5
45	9.03	7.95	9.25	8.55	7.75	9.83

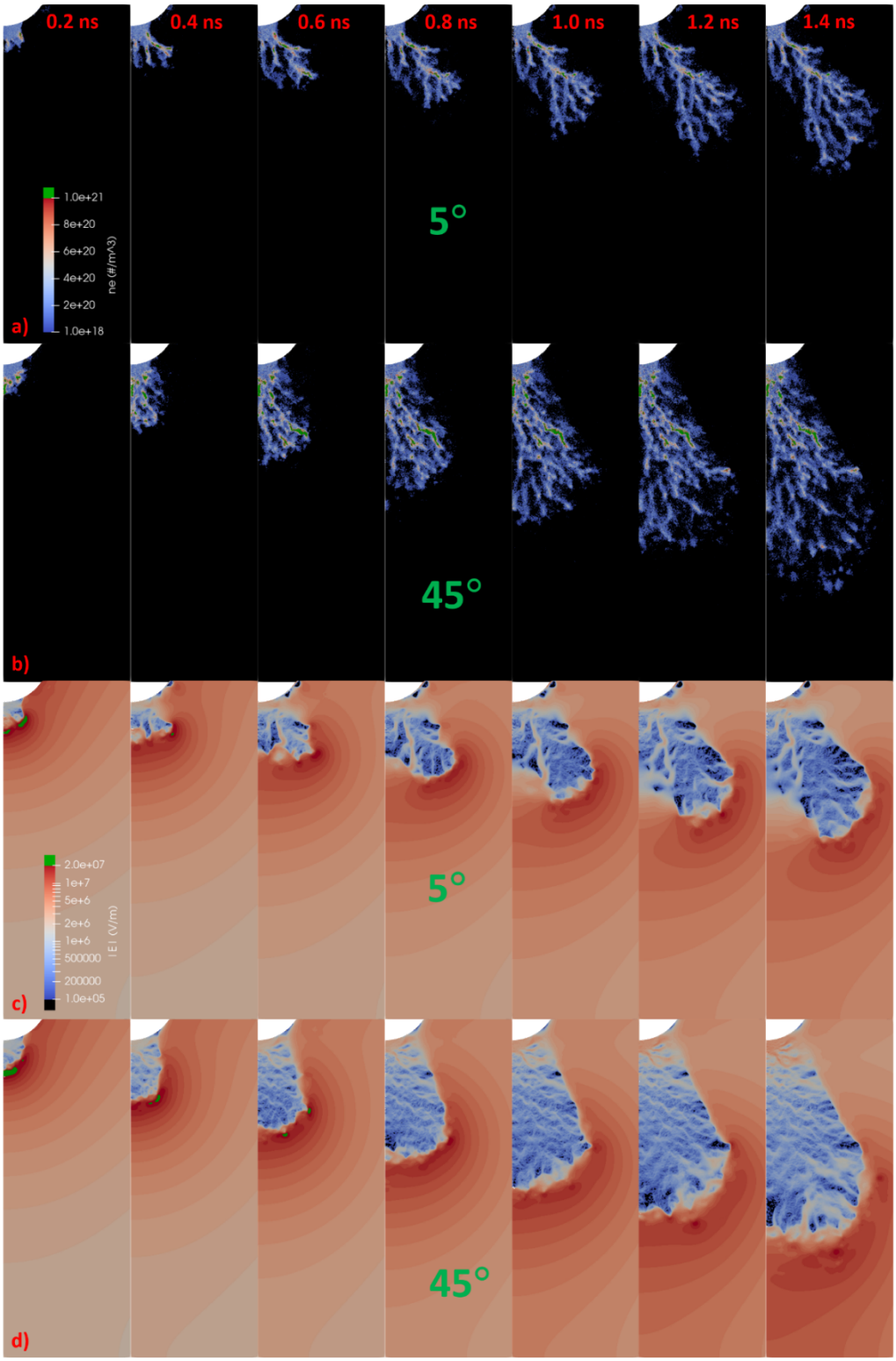

Figure 8. Temporal evolution of electron density (a and b) and electric field magnitude (c and d) of the near-field region (ie., $0 \leq r \leq 600$ μm of Figure 2) in *r-z* planes located at the midsection ($\phi/2$) of 5° (a and c) and 45° (b and d) wedges.

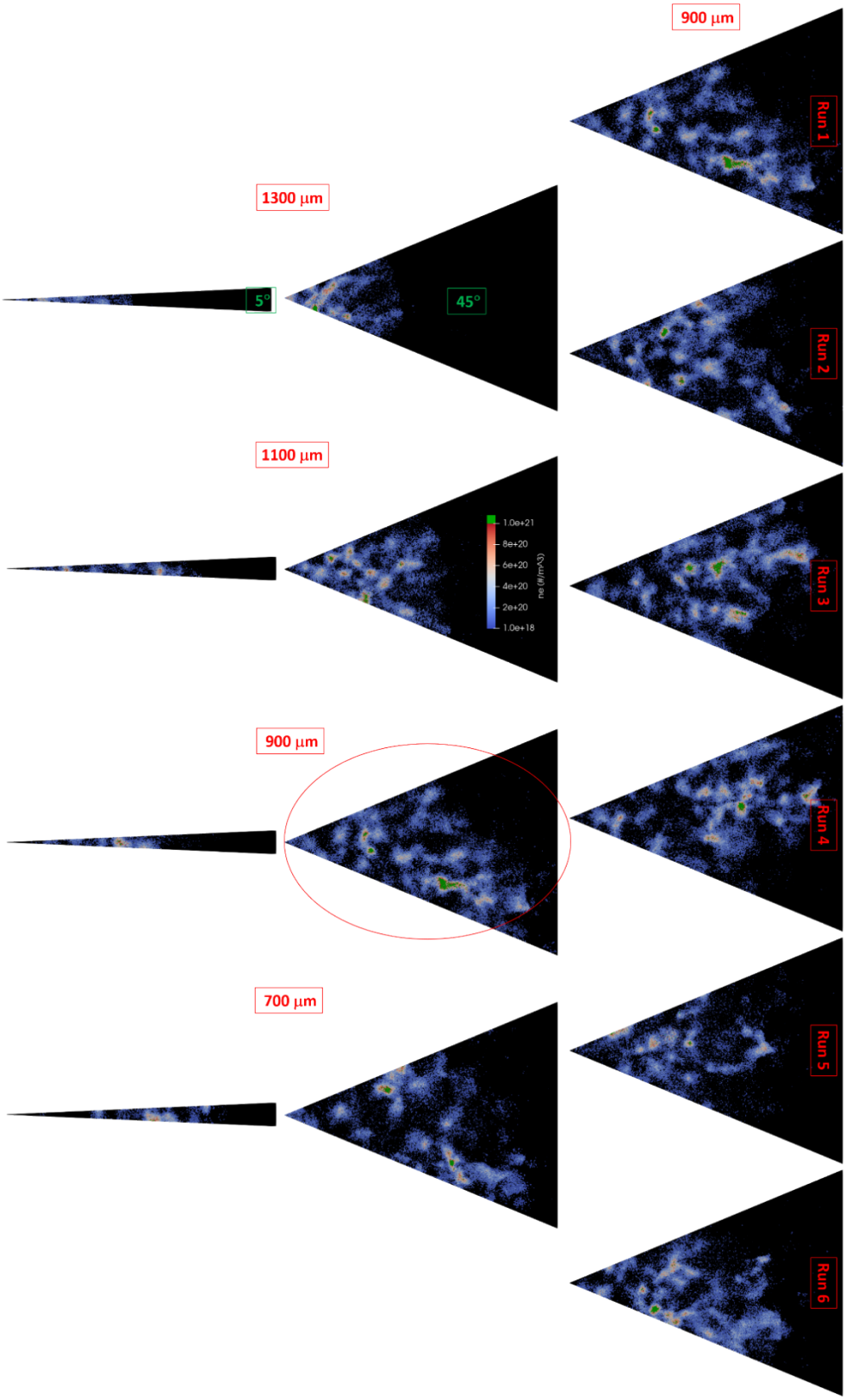

Figure 9. Electron density for 5° and 45° in *r-ϕ* planes located at 700, 900, 1100, and 1300 μm above the cathode (0 μm), at 1.4 nsec, coinciding with triangle positions shown in Error!

Reference source not found.. The 900 μm position highlighted at 45° is shown for all 6 simulations.

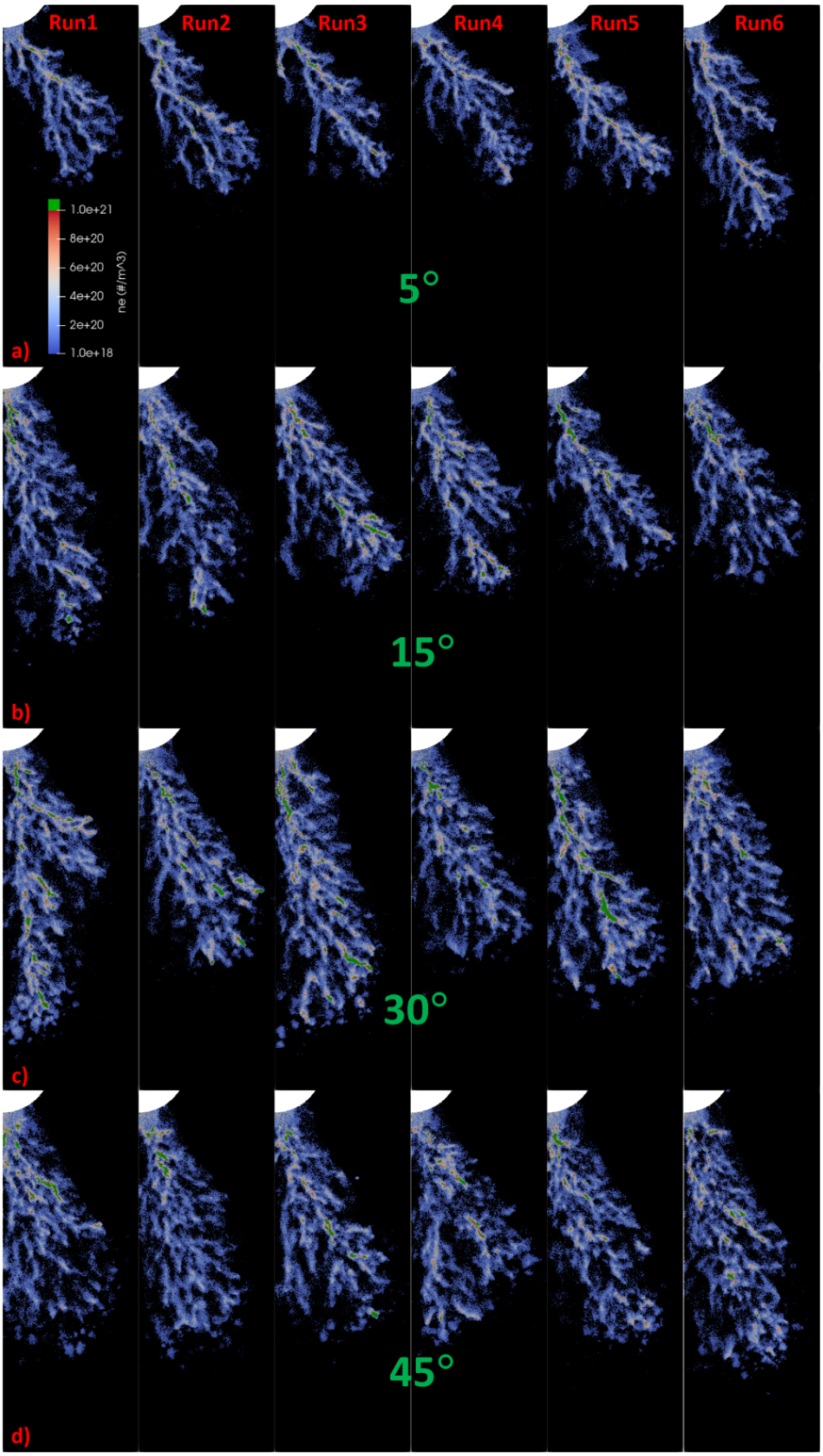

Figure 10. From top to bottom - electron densities of the near-field region (ie., $0 \leq r \leq 600$ μm of Figure 2) in *r-z* planes located at the midsection ($\phi/2$) of a) 5°, b) 15°, c) 30°, and d) 45° wedges at 1.4 nsec for all six randomly seeded simulations.

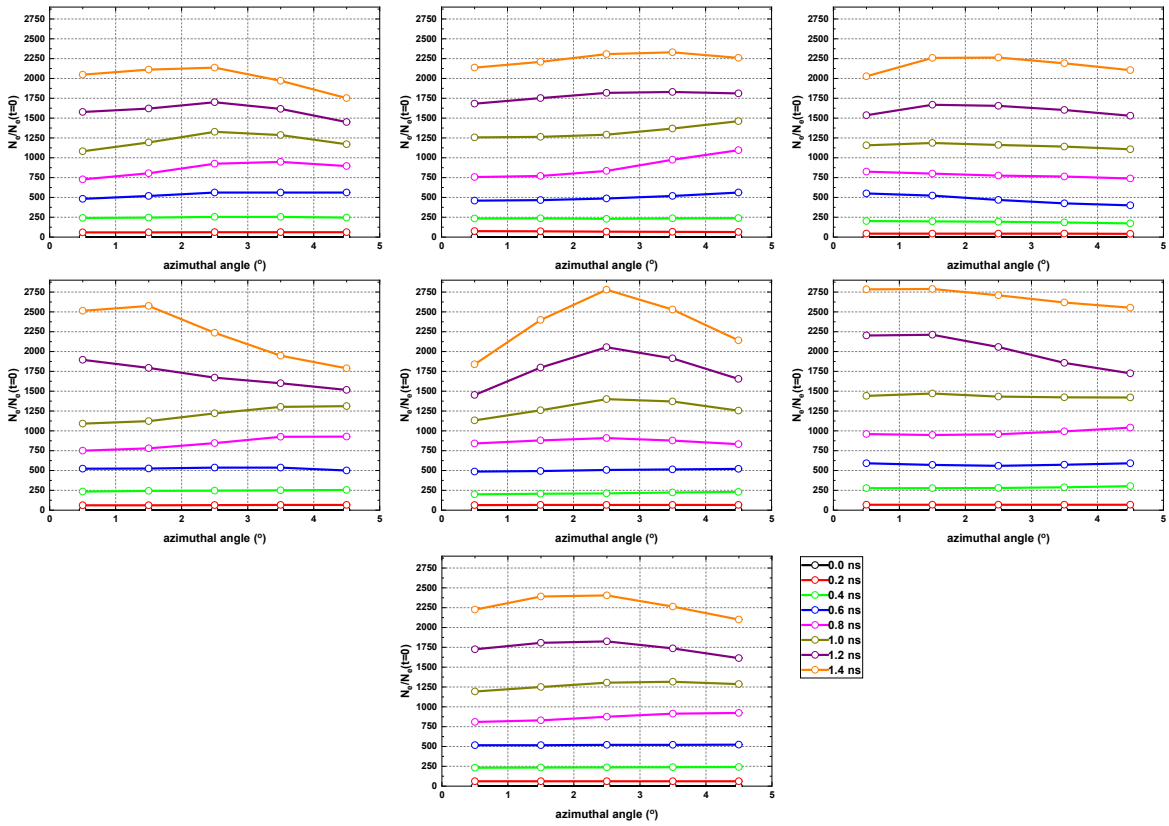

Figure 11. Ratio of the number of real electrons to the initial seed count at t = 0 for a 5° wedge as functions of time and spatial direction in ϕ, binned in 1 μm increments, where integration of electrons has been conducted in both r and z directions. The top six plots represent each of six randomly seeded simulations with bottom most plot representing the average.

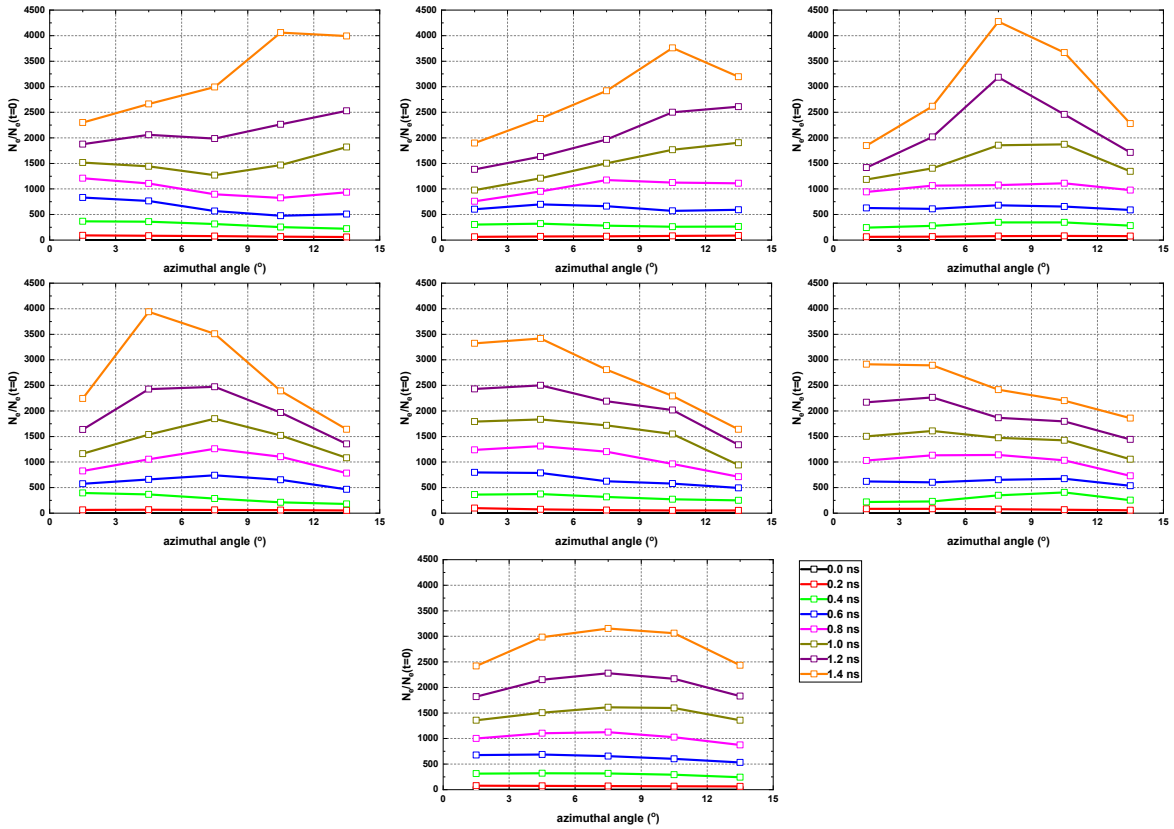

Figure 12. Ratio of the number of real electrons to the initial seed count at t = 0 for a 15° wedge as functions of time and spatial direction in ϕ, binned in 3 μm increments, where integration of electrons has been conducted in both r and z directions. The top six plots represent each of six randomly seeded simulations with bottom most plot representing the average.

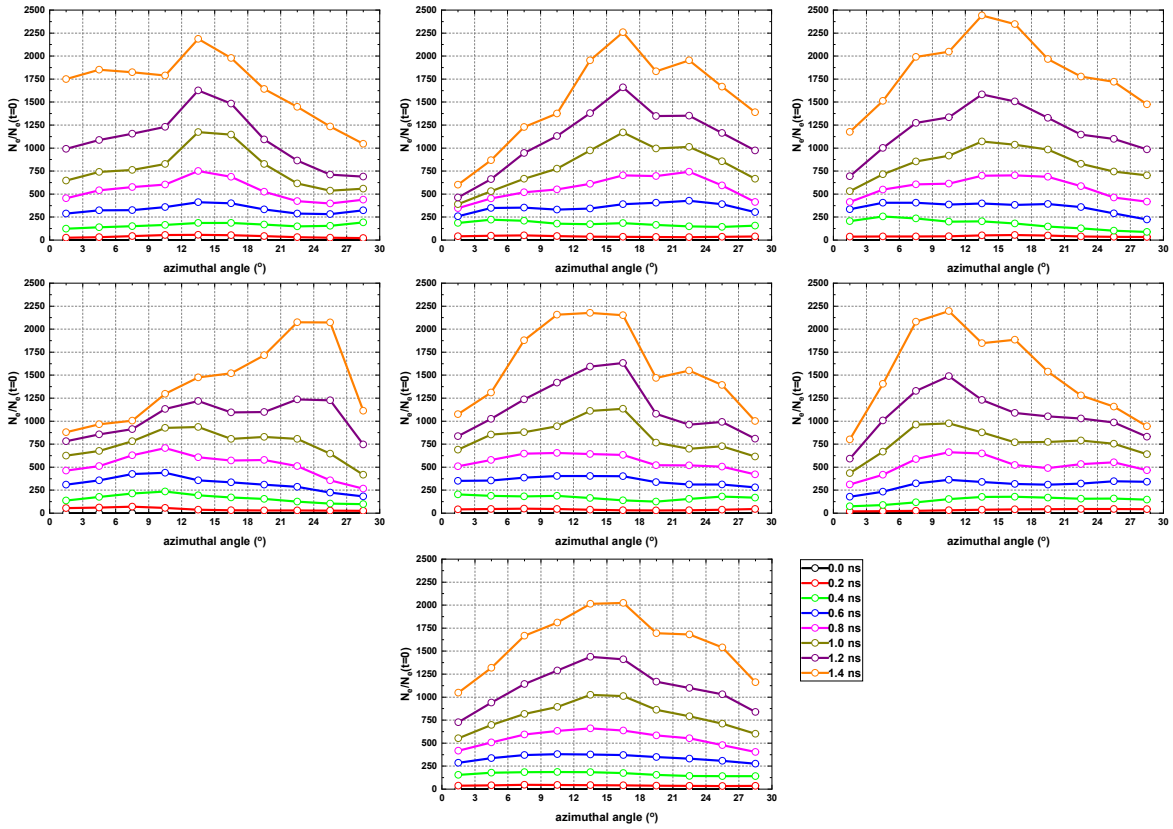

Figure 13. Ratio of the number of real electrons to the initial seed count at t = 0 for a 30° wedge as functions of time and spatial direction in ϕ, binned in 3 μm increments, where integration of electrons has been conducted in both r and z directions. The top six plots represent each of six randomly seeded simulations with bottom most plot representing the average.

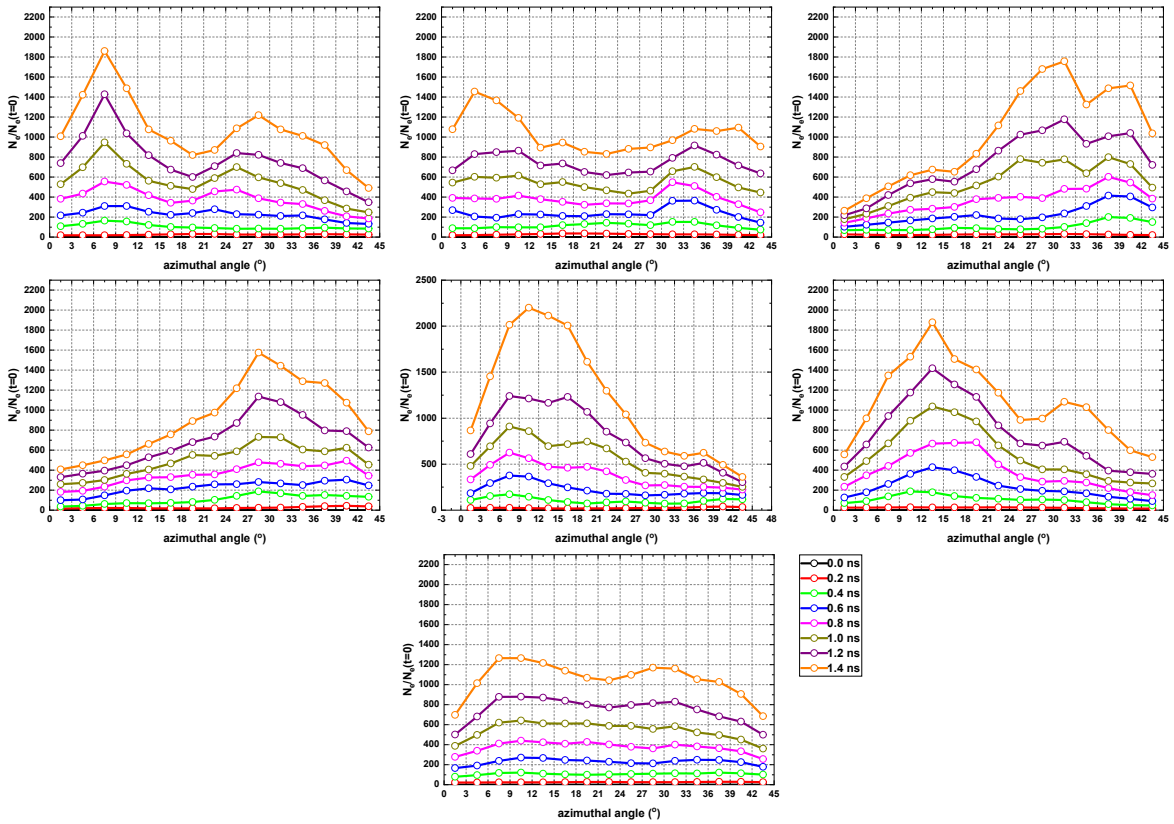

Figure 14. Ratio of the number of real electrons to the initial seed count at t = 0 for a 45° wedge as functions of time and spatial direction in ϕ, binned in 3 μm increments, where integration of electrons has been conducted in both r and z directions. The top six plots represent each of six randomly seeded simulations with bottom most plot representing the average.

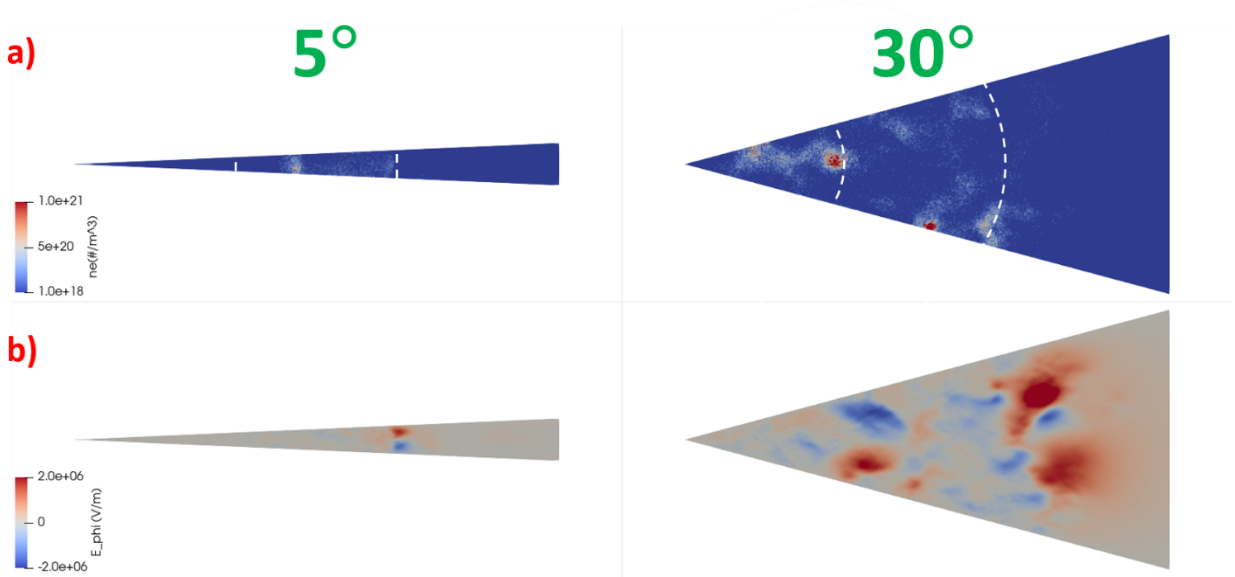

Figure 15. Electron density (a) and phi component of the electric field (b) for 5° (left column) and 30° (right column) wedges of the near-field region (ie., $0 \leq r \leq 600$ μm of Figure 2) of the *r-ϕ* plane located 900 μm above the cathode (0 μm), at 1.4 nsec. Radii at 200 and 400 μm have been delineated by white dashed arcs in (a).

4. CONCLUSIONS

We have applied fully kinetic 3D PIC-DSMC simulations of positive streamers, whereby all species (ie., photons, electrons, ions, and neutrals) were tracked as particles, and shown that variations in streamer growth dynamics exist when the domain is constrained to wedge angles of varying size to keep the problem space tractable. When streamer growth dynamics for wedge angles of 5°, 15°, 30°, and 45° were formally quantified in terms of average electron density and velocity, both temporally and spatially in r, ϕ, and z, results suggest that a wedge angle near 30° may be the minimum required for solution convergence, though future simulations will need to compare to 360° simulations to confirm this. Solution convergence here refers to the degree of deviation in these parameters. Relatively small deviation is observed between 30° and 45° wedges as the streamer evolves in time. On the contrary, the deviation in these parameters grows significantly with time between these wedge angles and the 5° case. The 15° case falls in between the 5° and 30°/45° cases, leaning towards the latter. Even though the deviation observed is less than the 5° wedge, we would only recommend a 15° angle if computational resources are severely limited, such that the trade-off between accuracy and computational costs are acceptable. Now, although electron densities were averaged over six randomly seeded independent simulations, this does not represent a statistically significant sample size. In the absence of a statistically large population to sample from, we can only infer from our results that a wedge near 30° is the minimum needed to allow streamers to evolve spatially in 3D without being adversely affected by the domain size.

The combination of qualitative and quantitative results, implemented through the projection of electric field and electron density on 2D slices in r-z and r-ϕ planes, along with temporal quantification of electron density in the form of spatially divided dz, dr, and $d\phi$ bins, respectively, suggest that a wedge angle as small as 15° may strike the balance between computational efficiency and the ability to model streamer physics in three dimensions with tolerable compromise in fidelity. However, the potential caveat to using such a restricted wedge angle is the arc length and associated ϕ-component of the field needed to resolve azimuthally oriented branching structures. If the added computational expense can be afforded, doubling the wedge angle to 30° may be the optimal choice to capture such branching phenomena. Furthermore, in order to provide further credence to this work, our future efforts will focus on three primary objectives: 1) simulations will be performed with true periodic boundaries, 2) the wedge angle will be expanded to 90°, 180°, and 360°, and 3) a larger sample of simulations will be acquired at each wedge angle. We anticipate a series of subsequent papers that will address these objectives and show that the results and conclusions presented here are either consistent with increasing population size and wedge angle, or need to be re-assessed, such that any additional computational expenses may have to be accepted.

REFERENCES

[1] C. Moore, A. Fierro, H. Hjalmarson, R. Jorgenson, M. Hopkins, L. Beidermann and P. Clem, "Development of Kinetic PIC-DSMC Model for Breakdown in the Presence of a Dielectric," in *International Conference on Plasma Science, https://www.osti.gov/servlets/purl/1366833*, Banff, Alberta, 2016.

[2] C. Moore, H. Hjalmarson, L. Beidermann, K. M. Williamson, P. A. Shultz and R. Jorgenson, "Development and Validation of PIC-DSMC Air Breakdown Model in the Presence of Dielectric Particles," in *Pulsed Power Conference*, Austin, TX., 2015.

[3] A. Fierro, J. Stephens, S. Beeson, J. Dickens and A. Neuber, "Discrete Photon Implementation for Plasma Simulations," *Physics of Plasmas,* vol. 23, no. 1, 2016.

[4] A. Jindal, C. Moore, A. Fierro and R. Jorgenson, "Streamer Formation Near a Dielectric Surface with Variable Quantum Efficiency," in *International Conference on Plasma Science*, Atlantic City, NJ., 2017.

[5] M. Ramesh, R. Summer and S. Singh, "Application of Streamer Criteria for Calculations of Flashover Voltages of Gaseous Insulation with a Solid Dielectric Barrier," in *Proceedings of 18th International Symposium on High Voltage Engineering*, Seoul, Korea, 2013.

[6] Y. Yang, A. Starikovskiy, A. Fridman and Y. Cho, "Analysis of Streamer Propagation for Electric Breakdown in Liquid/Bioliquid," *Plasma Medicine,* vol. 1, no. 1, 2011.

[7] H. Akiyama, "Streamer Discharges in Liquids and their Applications," *IEEE Transactions on Dielectrics and Electrical Insulation,* vol. 7, no. 5, 2000.

[8] A. Karpatne, D. Breden and L. Raja, "Simulations of Spark-Plug Transient Plasma Breakdown in Automotive Internal Combustion Engines," *SAE Technical Paper,* 2017.

[9] A. Y. Starikovskii, N. B. Anikin, I. N. Kosarev, E. I. Mintoussov, M. M. Nudnova, A. E. Rakitin, D. V. Roupassov, S. M. Starikovskaia and V. P. Zhukov, "Nanosecond-Pulsed Discharges for Plasma-AssistedCombustion and Aerodynamics," *Journal of Propulsion and Power,* vol. 24, 2008.

[10] W. Tie, C. Meng, Y. Zhang, Z. Yan and Q. Zhang, "Analysis on Discharge Process of a Plasma-Jet Triggered Gas Spark Switch," *Plasma Science and Technology,* vol. 20, no. 1, 2018.

[11] U. Ebert and D. Sentmen, "Streamers, Sprites, Leaders, Lightning: from Micro- to Macroscales," *Journal of Physics D: Applied Physics,* vol. 41, 2008.

[12] V. P. Pasko, "Theoretical Modeling of Sprites and Jets," in *Sprites, Elves and Intense Lightning Discharges*, New York, Springer, 2006, pp. 253-311.

[13] U. Ebert, S. Nijdam, C. Li, A. Luque, T. Briels and E. van Veldhuizen, "Review of recent results on streamer discharges and discussion of their relevance for sprites and lightning," *Journal of Geophysical Research - Space Physics,* vol. 115, 2010.

[14] Z. Bonaventura, A. Bourdon, S. Celestin and V. Pasko, "Electric field determination in streamer discharges in air at atmospheric pressure," *Plasma Sources Science and Technology,* vol. 20, 2011.

[15] G. Fridman, G. Friedman, A. Gutsol, A. B. Shekhter, V. N. Vasilets and A. Fridman, "Applied Plasma Medicine," *Plasma Processes and Polymers,* vol. 5, no. 6, 2008.

[16] T. M. P. Briels, J. Kos, G. J. J. Winands, E. M. van Veldhuizen and U. Ebert, "Positive and negative streamers in ambient air: measuring diameter, velocity, and dissipated energy," *Journal of Physics D: Applied Physics,* vol. 41, 2008.

[17] B. Bagheri and J. Teunissen, "The effect of the stochasticity of photoionization on 3D streamer simulations," *Plasma Sources Science and Technology,* vol. 28, 2019.

[18] A. Luque, U. Ebert and W. Hundsdorfer, "Interaction of Streamer Discharges in Air and Other Oxygen-Nitrogen Mixtures," *Physical Review Letters,* vol. 101, no. 7, 2008.

[19] L. Papageorgiou, A. C. Metaxas and G. E. Georghiou, "Three-dimensional numerical modelling of gas discharges at atmospheric pressure incorporating photoionization phenomena," *Journal of Physics D: Applied Physics,* vol. 44, 2011.

[20] J. Teunissen and U. Ebert, "Simulating streamer discharges in 3D with the parallel adaptive Afivo framework," *Journal of Physics D: Applied Physics,* 2017.

[21] S. Nijdam, J. Teunissen, E. Takahashi and U. Ebert, "The role of free electrons in the guiding of positive streamers," *Plasma Sources Science and Technology,* vol. 25, 2016.

[22] R. Marskar, "Adaptive multiscale methods for 3D streamer discharges in air," *Plasma Research Express,* vol. 1, 2019.

[23] M. Jiang, Y. Li, H. Wang and C. Liu, "3D PIC-MCC simulations of positive streamers in air gaps," *Physics of Plasmas,* vol. 24, 2017.

[24] A. Sun, J. Teunissen and U. Ebert, "3-D Particle Modeling of Positive Streamer Inception From a Needle Electrode in Supercritical Nitrogen," *IEEE Transactions on Plasma Science,* vol. 42, no. 10, 2014.

[25] J. Teunissen and U. Ebert, "3D PIC-MCC simulations of discharge inception around a sharp anode in nitrogen/oxygen mixtures," *Plasma Sources Science and Technology,* vol. 25, 2016.

[26] S. Nijdam, E. Takahashi, J. Teunissen and U. Ebert, "Streamer discharges can move perpendicularly to the electric field," *New Journal of Physics,* vol. 16, 2014.

[27] O. Chanrion and T. Neubert, "A PIC-MCC code for simulation of streamer propagation in air," *Journal of Computational Physics,* vol. 227, no. 15, 2008.

[28] C. Li, J. Teunissen, M. Nool, W. Hundsdorfer and U. Ebert, "A comparison of 3D particle, fluid, and hybrid simulations for negative streamers," *Plasma Sources Science and Technology,* vol. 21, 2012.

[29] C. Li, U. Ebert and W. Hundsdorfer, "3D hybrid computations for streamer discharges and production of run-away electrons," *Journal of Physics D: Applied Physics,* vol. 42, 2009.

[30] C. Li, U. Ebert and W. Hundsdorfer, "Spatially hybrid computations for streamer discharges: II. Fully 3D simulations," *Journal of Computational Physics,* vol. 231, 2010.

[31] J.-M. Plewa, O. Eichwald, P. Ducasse, C. Jacobs, N. Renon and M. Yousfi, "3D streamers simulation in a pin to plane configuration using massively parallel computing," *Journal of Physics D: Applied Physics,* vol. 51, 2018.

[32] D. Rose, D. R. Welch, R. E. Clark, C. Thomas, W. R. Zimmerman, N. Bruner, P. K. Rambo and B. W. Atherton, "Towards a fully kinetic 3D electromagnetic particle-in-cell model of streamer formation and dynamics in high-pressure electronegative gases," *Physics of Plasmas,* vol. 18, 2011.

[33] A. Fierro, C. Moore, B. Yee and M. Hopkins, "Three-dimensional kinetic modeling of streamer propagation in a nitrogen/helium gas mixture," *Plasma Sciences Sources and Technology,* vol. 27, no. 10, 2018.

[34] Z. Eckert, R. Hopper, M. Bettencourt, J. J. Boerner, P. Crozier, S. Dirk, A. Fierro, A. M. Grillet, T. Hughes, H. Meyer, C. Moore, S. Moore, L. Musson, S. Plimpton, N. Roberds, A. Williams, J. L. Pacheco and M. M. Hopkins, "Aleph: Highly Scalable Dynamically Load Balanced Unstructured PIC-DSMC Low Temperature Plasma Code," 2022.

[35] C. K. Birdsall and A. B. Langdon, Plasma Physics via Computer Simulation, vol. 27, CRC Press, 2004.

[36] G. A. Bird, Molecular Gas Dynamics and the Direct Simulation of Gas Flows, Oxford, 1994.

[37] B. M. Smirnov, "Tables for cross sections of the resonant charge exchange process," *Physica Scripta,* vol. 61, pp. 595-602, 2000.

[38] A. Okhrimovskyy, A. Bogaerts and R. Gijbels, "Electron anistropic scattering in gases: A formula fo Monte Carlo simulations," *Physical Review E,* vol. 65, 2002.

[39] D. P. Schmidt and C. J. Rutland, "A New Droplet Collision Algorithm," *Journal of Computational Physics,* vol. 164, no. 1, 2000.

[40] C. Moore, A. Jindal, A. Fierro, K. Cartwright and M. Hopkins, "PIC-DSMC numerical grid heating in collisional plasmas: Application to streamer discharge simulations," in *IEEE Pulsed Power & Plasma Science Conference, https://www.osti.gov/servlets/purl/1640960*, Orlando, 2019.

[41] J. Qin and V. P. Pasko, "On the propagation of streamers in electrical discharges," *Journal of Physics D: Applied Physics,* vol. 47, 2014.

[42] S. Nijdam, F. M. J. H. van der Wetering, R. Blanc, E. M. van Veldhuizen and U. Ebert, "Probing photo-ionization: experiments on positive streamers in pure gases and mixtures," *Journal of Physics D: Applied Physics,* vol. 43, 2010.

[43] R. Morrow and J. J. Lowke, "Streamer propagation in air," *Journal of Physics D: Applied Physics,* vol. 30, 1997.

[44] T. M. P. Briels, E. M. van Veldhuizen and U. Ebert, "Positive streamers in air and nitrogen of varying density: experiments on similarity laws," *Journal of Physics D: Applied Physics,* vol. 41, 2008.

This page left blank

APPENDIX A. UNCERTAINTY VALUES IN R AND Z COORDINATES

Table A-1. Values of uncertainty in the ratio of total real electrons to the value at *t* = 0 as functions of the *z*-coordinate direction and time, for all wedge angles, represented as absolute minimum and maximum values. In each number set (3 rows x 4 columns), the values from left to right in a single row, each separated by a forward slash, correspond to 5°, 15°, 30°, and 45° wedge angles, respectively. The top, middle, and bottom rows in each number set correspond to the minimum, average, and maximum, respectively, each taken over 6 simulations. Values with two or more zeros after the decimal are rounded down to 0.

z (μm)	0.2 ns	0.6 ns	1.0 ns	1.4 ns
75	213/307/351/362	861/844/794/749	912/864/809/766	928/890/850/811
	307/358/394/375	1110/915/869/800	1140/939/889/817	1150/974/942/863
	346/382/420/403	1320/993/923/861	1350/1010/947/874	1360/1050/1040/919
225	.035/.059/.019/.219	1220/1150/1250/1470	1500/1230/1330/1560	1510/1240/1340/1570
	.111/.204/.851/.511	1370/1580/1550/1580	2250/1870/1750/1750	2320/1890/1760/1760
	.286/.446/3.35/.98	1540/1820/1780/1800	2850/2270/2060/2090	3080/2280/2080/2100
375	0/0/0/0	2/396/635/707	1840/2030/1670/1970	2270/2130/1710/2010
	0/0/0/0	117/648/907/1030	2270/2370/2040/2240	2850/2520/2120/2310
	.0172/0/0/0	330/1090/1290/1140	3130/2980/2360/2400	3530/3090/2430/2520
525	0/0/0/0	0/.243/.943/.53	91.5/1420/1780/1920	1740/2170/2180/2720
	0/0/0/0	.0808/2.68/57.3/7.88	623/1870/2180/2380	3060/3070/2750/3060
	0/0/0/0	.339/14/166/20.7	1580/2380/2540/2700	4490/3980/3320/3300
675	0/0/0/0	0/0/.0146/0	0.0175/45.8/242/240	675/2260/2000/2620
	0/0/0/0	0/.011/.0318/.0183	72.3/37/1030/925	1550/2990/2880/3200
	0/0/0/0	.0175/.0292/.075/.0253	432/1390/1840/1520	3420/4370/3510/3680
825	0/0/0/0	0/0/0/0	0/.0565/.412/.435	0.111/381/1690/1400
	0/0/0/0	0/0/0/0	.0448/3.19/82.4/15.7	436/1760/2830/2540
	0/0/0/0	0/0/0/0	.158/17.8/359/71.3	2600/2980/3650/2970
975	0/0/0/0	0/0/0/0	0/0/0/0	0/1.14/96.4/484
	0/0/0/0	0/0/0/0	0/.0133/.0827/.0247	17.1/705/1700/1790
	0/0/0/0	0/0/0/0	0/.0542/.382/.0487	102/2880/3510/3670
1125	0/0/0/0	0/0/0/0	0/0/0/0	0/0/1.3/2.11
	0/0/0/0	0/0/0/0	0/0/0/0	.0146/158/880/276
	0/0/0/0	0/0/0/0	0/0/0/0	.0818/943/2650/1460
1275	0/0/0/0	0/0/0/0	0/0/0/0	0/0/0/0
	0/0/0/0	0/0/0/0	0/0/0/0	0/.437/98.9/.568
	0/0/0/0	0/0/0/0	0/0/0/0	0/2.5/351/2.66
1425	0/0/0/0	0/0/0/0	0/0/0/0	0/0/0/0
	0/0/0/0	0/0/0/0	0/0/0/0	0/0/.599/.0464
	0/0/0/0	0/0/0/0	0/0/0/0	0/.0117/2.51/.257

Table A-2. Values of uncertainty in the ratio of total real electrons to the value at *t* = 0 as functions of the *r*-coordinate direction and time, for all wedge angles, represented as absolute minimum and maximum values. In each number set (3 rows x 4 columns), the values from left to right in a single row, each separated by a forward slash, correspond to 5°, 15°, 30°, and 45° wedge angles, respectively. The top, middle, and bottom rows in each number set correspond to the minimum, average, and maximum, respectively, each taken over 6 simulations. Values with two or more zeros after the decimal are rounded down to 0.

r (μm)	0.2ns	0.6ns	1.0ns	1.4ns
50	201/295/334/340	431/777/925/918	448/893/1010/1120	452/911/1070/1260
	287/345/377/358	657/1000/1280/1120	688/1130/1570/1290	699/1190/1810/1430
	324/372/405/391	834/1450/1640/1230	900/1790/2070/1470	912/1890/2370/1570
150	5.27/7.73/11.7/12.6	1300/1590/1590/1840	1570/2179/2520/2600	1610/2220/2800/3070
	19.5/12.5/17.6/16.8	1480/1760/1770/1940	2070/2610/2940/3040	2160/2770/4060/3530
	37.7/16.6/29.1/21.8	1700/1880/2030/2070	3100/3000/3640/3400	3260/3330/6610/3820
250	0/.228/.2/.122	160/112/81.9/203	2010/2260/2190/2490	2110/2740/3660/3350
	1.31/.498/.272/.655	460/388/337/351	2330/2540/2600/2660	2800/4210/4430/4200
	4.4/.971/.405/1.56	831/538/593/614	2500/2820/2880/2870	3690/5870/5640/4970
350	0/0/0/.013	.28/.477/.445/.633	716/400/314/656	2820/3020/2210/2970
	0/.0237/.0164/.0371	1.07/1.11/.859/.902	1250/1120/849/1130	3480/3590/3800/4280
	.0172/.0562/.0341/.0812	2.74/2.08/1.21/1.26	1870/1970/1430/1320	4670/4170/4610/5680
450	0/0/0/0	.035/.0331/.0564/.0506	2.29/.716/.922/2.86	934/739/709/1800
	0/0/0/0	.0691/.0678/.0709/.0913	16.7/34.4/7.57/15.9	2080/1910/1780/2060
	0/0/.0172/0	.105/.13/.0876/.2	43.5/172/27.6/39	2750/3180/2770/2510
550	0/0/0/0	0/0/.0127/0	.158/.15/.119/.125	4.06/2.11/3.64/19.4
	0/0/0/0	.0166/.0139/.0177/.0264	.276/.24/.149/.203	171/373/92.9/307
	0/0/0/0	.0292/.0311/.0243/.0648	.449/.471/.182/.248	578/1000/259/716

DISTRIBUTION

Email—Internal

Name	Org.	Sandia Email Address
Richard Kramer	01351	rmkrame@sandia.gov
Ben Long	02934	benlong@sandia.gov
Technical Library	01977	sanddocs@sandia.gov

This page left blank

This page left blank

Sandia National Laboratories

Sandia National Laboratories is a multimission laboratory managed and operated by National Technology & Engineering Solutions of Sandia LLC, a wholly owned subsidiary of Honeywell International Inc. for the U.S. Department of Energy's National Nuclear Security Administration under contract DE-NA0003525.